

Elemental Abundances in M31: The Kinematics and Chemical Evolution of Dwarf Spheroidal Satellite Galaxies*

EVAN N. KIRBY,¹ KAROLINE M. GILBERT,^{2,3} IVANNA ESCALA,^{1,4} JENNIFER WOJNO,³ PURAGRA GUHATHAKURTA,⁵
STEVEN R. MAJEWSKI,⁶ AND RACHAEL L. BEATON^{4,7,†}

¹California Institute of Technology, 1200 E. California Blvd., MC 249-17, Pasadena, CA 91125, USA

²Space Telescope Science Institute, 3700 San Martin Dr., Baltimore, MD 21218, USA

³Department of Physics & Astronomy, Bloomberg Center for Physics and Astronomy, Johns Hopkins University, 3400 N. Charles Street, Baltimore, MD 21218

⁴Department of Astrophysical Sciences, Princeton University, 4 Ivy Lane, Princeton, NJ 08544

⁵Department of Astronomy & Astrophysics, University of California, Santa Cruz, 1156 High Street, Santa Cruz, CA 95064, USA

⁶Department of Astronomy, University of Virginia, Charlottesville, VA 22904-4325, USA

⁷The Observatories of the Carnegie Institution for Science, 813 Santa Barbara St., Pasadena, CA 91101

(Accepted 3 December 2019)

Submitted to AJ

ABSTRACT

We present deep spectroscopy from Keck/DEIMOS of Andromeda I, III, V, VII, and X, all of which are dwarf spheroidal satellites of M31. The sample includes 256 spectroscopic members across all five dSphs. We confirm previous measurements of the velocity dispersions and dynamical masses, and we provide upper limits on bulk rotation. Our measurements confirm that M31 satellites obey the same relation between stellar mass and stellar metallicity as Milky Way (MW) satellites and other dwarf galaxies in the Local Group. The metallicity distributions show similar trends with stellar mass as MW satellites, including evidence in massive satellites for external influence, like pre-enrichment or gas accretion. We present the first measurements of individual element ratios, like [Si/Fe], in the M31 system, as well as measurements of the average $[\alpha/\text{Fe}]$ ratio. The trends of $[\alpha/\text{Fe}]$ with [Fe/H] also follow the same galaxy mass-dependent patterns as MW satellites. Less massive galaxies have more steeply declining slopes of $[\alpha/\text{Fe}]$ that begin at lower [Fe/H]. Finally, we compare the chemical evolution of M31 satellites to M31's Giant Stellar Stream and smooth halo. The properties of the M31 system support the theoretical prediction that the inner halo is composed primarily of massive galaxies that were accreted early. As a result, the inner halo exhibits higher [Fe/H] and $[\alpha/\text{Fe}]$ than surviving satellite galaxies.

1. INTRODUCTION

1.1. Formation of Stellar Halos

Dwarf galaxies have been established as the building blocks of stellar halos. Theoretical simulations (e.g., Bullock & Johnston 2005; Johnston et al. 2008) predict that more massive dwarf galaxies were accreted early in the formation of an L_* galaxy. As a result,

their stars populate the inner portions ($r \lesssim 30$ kpc) of the halo. Less massive dwarf galaxies contribute later, sometimes dissolving into tidal streams. Observational evidence in the Milky Way (MW) supports these predictions. Proper motions from the *Gaia* satellite have discovered MW field stars that probably belonged originally to a now-accreted galaxy, dubbed Gaia-Enceladus, with a stellar mass of $\sim 6 \times 10^8 M_\odot$ (Belokurov et al. 2018; Helmi et al. 2018). The MW also shows evidence of more recent accretion of smaller satellites, like the Sagittarius dwarf spheroidal galaxy (dSph), which has a stellar mass of $\sim 10^8 M_\odot$ (Niederste-Ostholt et al. 2010) and is embedded in a well-defined tidal stream (Ibata et al. 1994; Majewski et al. 2003).

The elemental abundances of stars help disentangle the accretion histories of stellar halos. Detailed abun-

Corresponding author: Evan N. Kirby
enk@astro.caltech.edu

* The data presented herein were obtained at the W. M. Keck Observatory, which is operated as a scientific partnership among the California Institute of Technology, the University of California and the National Aeronautics and Space Administration. The Observatory was made possible by the generous financial support of the W. M. Keck Foundation.

† Hubble Fellow, Carnegie-Princeton Fellow

dance ratios, like $[\text{O}/\text{Fe}]^1$ and $[\text{Mg}/\text{Fe}]$, are lower in metal-poor ($[\text{Fe}/\text{H}] \lesssim -1$) stars in MW dSphs compared to the MW halo (Shetrone et al. 2001, 2003; Venn et al. 2004; Hayes et al. 2018). This observation affirms that the majority of the stellar mass of the MW halo was built of systems with different chemical evolution histories from the presently surviving dSph satellites. Even the bulk metallicities of stars are informative because dwarf galaxies obey a universal relationship between stellar mass and stellar metallicity (Mateo 1998; Grebel et al. 2003; Kirby et al. 2011b, 2013, hereafter K13). Therefore, the metallicity distribution of the halo can be used to estimate the mass function of accreted galaxies. Observationally, the metallicities—like the kinematics—suggest that the majority of stars come from more massive dwarf galaxies ($M_* \sim 10^8 M_\odot$, Deason et al. 2015, 2016; Lee et al. 2015).

While the MW has provided a trove of kinematical and abundance information from photometry, spectroscopy, and astrometry, it is only a single galaxy in a Universe filled with cosmic variance. In fact, the MW may be unusual in several regards. For example, most MW-like galaxies lack a satellite with the luminosity of the Large Magellanic Cloud ($1.5 \times 10^9 L_\odot$, de Vaucouleurs et al. 1991), and even fewer have two Magellanic-type satellites (Tollerud et al. 2011; Busha et al. 2011). Furthermore, the Local Group is unusual for having so few star-forming satellites (Geha et al. 2017). There is also tentative evidence that the MW halo is lower in stellar mass and more metal-poor than halos of mass similar to the MW (Monachesi et al. 2016; Brauer et al. 2019). We can achieve a more complete view of galaxy assembly and evolution by examining the halo and satellites of galaxies other than the MW.

The Great Andromeda Galaxy (M31) is an obvious alternative to the MW. The entire M31 system is confined to a portion of the sky, as opposed to the MW, which occupies the entire sky. At the same time, its proximity (785 kpc, McConnachie et al. 2005) still permits detailed observations, including resolved stellar spectroscopy. M31 also is a good laboratory for hierarchical formation because it hosts dozens of satellite galaxies (i.a., McConnachie 2012), and it has several prominent tidal streams (Ibata et al. 2001, 2014; Richardson et al. 2011).

This paper is part of a series on the elemental abundances of individual stars in the halo, Giant Stellar Stream (GSS), outer disk, and dwarf satellite galaxies of M31. Escala et al. (2019b) presented detailed abundance ratios of 11 stars in M31’s smooth halo. Gilbert

et al. (2019) showed similar measurements for 21 stars in the GSS, along with a comparison to the abundances of dwarf galaxies. Escala et al. (2019a) expanded the sample to 70 additional stars in M31’s smooth halo, kinematically cold substructure, and outer disk. They also performed a comparative analysis between the structural components of M31, including a comparison of the inner stellar halo to M31 dSphs. This paper presents spectroscopy of 256 member stars in five M31 satellite galaxies. The sample includes measurements of $[\text{Fe}/\text{H}]$ for 241 stars and $[\alpha/\text{Fe}]$ for 163 stars. We discuss our spectroscopic observations and measurements in Section 2.

1.2. Learning About Dwarf Galaxies from Resolved Stellar Spectroscopy

In addition to its utility in probing the signatures of hierarchical formation, our sample is also useful for studying the properties of dwarf galaxies for their own sake. For example, the radial velocities of stars in dwarf galaxies can be used in complementarity with metallicities to infer the masses and formation histories of those galaxies. (See Kalirai et al. 2009, 2010, Tollerud et al. 2012, and Collins et al. 2013 for past kinematic studies of M31 dSphs.) Radial velocities can also reveal the presence of rotation or kinematic substructure. We discuss the kinematic properties of the M31 dSphs in Section 3.

The metallicities of stars in a galaxy encode the galaxy’s history of nucleosynthesis, star formation, and gas flow (Tinsley 1980). Each galactic component in which the metals are measured provides complementary information. The composition of the cold interstellar medium reflects the metals available for new star formation. Metals in the warm circumgalactic medium have been expelled from past episodes of gas outflow. Finally, metals in stars record the history of chemical evolution. The stellar metallicity distribution function (MDF) is the product of the star formation history (SFH) with the age–metallicity relation: $dM_*/dZ_* = dM_*/dt \times dt/dZ_*$, where M_* represents the stellar mass at time t , and Z_* represents the stellar metallicity.

Even the average stellar metallicity of the galaxy (the zeroth moment of the MDF) is informative. For gas-free galaxies, like the dSphs under consideration here, the stellar MDF represents all of the metals the galaxy has retained. In other words, it is the difference between all the metals created by stars and all of the metals lost due to outflows or stripping. To first order, metal creation is a function of stellar mass. (More stars will make more metals.) Metal outflow is a function of the gravitational potential. (A deeper potential allows the galaxy to retain more metals.) This simple description explains the mass–metallicity relation (MZR) for dwarf galaxies (Lequeux et al. 1979; Skillman et al. 1989; Kirby et al. 2011b; K13). Galaxies with low M_* also have low Z_* , which indicates that they retained a smaller fraction of the metals created by their stars than galaxies with

¹ We use the notation $[A/B] = \log[n(A)/n(B)] - \log[n_\odot(A)/n_\odot(B)]$, where $n(A)$ is the number density of atom A. In this paper, we use the solar abundances of Anders & Grevesse (1989) except in the case of Fe, for which $\epsilon(\text{Fe}) = 12 + \log[n(\text{Fe})/n(\text{H})] = 7.52$.

high M_* (Kirby et al. 2011c). We discuss the particular case of the metallicities of the M31 dSphs in Section 4.

In the beginning of a galaxy’s life, the only type of supernova to explode is core collapse (e.g., Type II). Core collapse supernovae produce a high ratio of the abundances of α elements, like O and Mg, to iron. As the galaxy progresses in its chemical evolution, Type Ia supernovae explode and produce copious amounts of iron but a small amount of α elements. As a result, the $[\alpha/\text{Fe}]$ ratio of a galaxy generally declines over time. Bursts of star formation can temporarily enhance $[\alpha/\text{Fe}]$ because the accompanying core collapse supernovae eject large amounts of α elements. However, dwarf galaxies are particularly susceptible to a steep decline in $[\alpha/\text{Fe}]$ vs. $[\text{Fe}/\text{H}]$. First, dwarf galaxies generally have very low star formation rates (SFRs), as revealed through direct observations of star-forming dwarfs (Lee et al. 2009) and measurements of the SFHs of quiescent dwarfs (Dolphin 2002; Weisz et al. 2014). Second, their chemical evolution is slow. For example, the rate at which $[\text{Fe}/\text{H}]$ increased in Local Group satellite galaxies was probably slower than in the primary progenitors of the halos of the MW or M31 (Robertson et al. 2005; Font et al. 2006; Johnston et al. 2008).

The chemical evolution of MW satellite galaxies has been documented extensively (e.g., Suntzeff et al. 1993; Shetrone et al. 1998, 2001, 2003; Geisler et al. 2005; Kirby et al. 2009, 2011a; Tolstoy et al. 2009; Letarte et al. 2010; Lemasle et al. 2014; Hill et al. 2019). In contrast, the measurements of detailed abundances of individual stars outside of the MW’s virial radius has been limited by the stars’ faintness. So far, the only measurements of $[\alpha/\text{Fe}]$ outside of the MW’s virial radius are for stars in M31’s dSphs and halo (Vargas et al. 2014a, hereafter V14a; Vargas et al. 2014b; Gilbert et al. 2019; Escala et al. 2019a,b) and stars in a few Local Group dIrrs (Kirby et al. 2017). This paper expands the body of detailed abundance measurements in M31 dSphs, including measurements of individual element ratios, such as $[\text{Si}/\text{Fe}]$. Section 5 presents our contribution to the study of detailed abundances in M31 dSphs.

After we discuss the properties of the satellites themselves, we return to their role in the assembly of M31’s stellar halo in Section 6. Finally, we summarize the paper in Section 7.

2. SPECTROSCOPY

We obtained spectroscopy with Keck/DEIMOS (Faber et al. 2003) of individual red giants in five dSphs: Andromeda VII, I, III, V, and X. They are numbered in the order in which they were discovered: And I and III (van den Bergh 1972), And V (Armandroff et al. 1998), And VII (Karachentsev & Karachentseva 1999), and And X (Zucker et al. 2007). However, in this paper, we list them in decreasing order of stellar mass whenever they appear in a list (e.g., in tables and in figures).

2.1. Target Selection

The deep spectroscopic slitmasks were designed using results from slitmasks previously observed for approximately one hour as part of the Spectroscopic Landscape of Andromeda’s Stellar Halo survey (SPLASH, e.g., Guhathakurta et al. 2006; Gilbert et al. 2009, 2012). These masks, obtained by Kalirai et al. (2009, 2010) and Tollerud et al. (2012), were based on photometry obtained by Grebel & Guhathakurta (1999, And VII), Ostheimer (2003, And I and III), Beaton (2014, And V), and Zucker et al. (2007, And X). However, the photometry used to design slitmasks presented in this paper is exclusively from the Mosaic imager at Kitt Peak National Observatory. The photometry was obtained by Beaton (2014) in the Washington system (M and T_2 filters), which we transformed to the Cousins system (V and I filters) following Majewski et al. (2000). Images were also obtained with the DDO51 filter. The DDO51 bandpass contains the Mg b triplet, which is a feature sensitive to surface gravity, and the $M - \text{DDO51}$ color then serves as a photometric proxy to distinguish dwarfs and giants of the same $M - T_2$ color. The previous slitmasks (with shallower observations) used this diagnostic to select against foreground dwarf stars, which have stronger Mg b triplets than red giant branch (RGB) stars.

As with most imaging spectrographs, the design of DEIMOS slitmasks required us to choose some targets for spectroscopy at the expense of others. We developed a priority scheme to maximize the number of dSph members. Stars identified from previous slitmasks as likely to be RGB stars at the distance of the dSph were included on the mask with highest priority, while objects previously identified as MW foreground stars or background galaxies were given lowest priority in the target list. High priority was also given to M31 dSph stars with existing literature abundance measurements (V14a). Additional spectroscopic targets were chosen using the prioritization applied for the SPLASH survey masks, which prioritized stars near the tip of the RGB of each dSph over stars above or significantly below the tip. Finally, we drew a wide polygon in the color–magnitude diagram (CMD) around the RGB for each dSph, as shown in Figure 1. Stars outside of the polygons were given low priority for target selection. The polygons were drawn so that any star that could reasonably belong to the RGB was included.

Figure 1 shows the CMDs of the five dSphs. Figure 2 shows the orientation of the slitmasks on the sky. Stars confirmed to be spectroscopic members, as described in Section 2.5, are indicated by purple circles in both figures.

2.2. Observations and Data Reduction

We observed the five M31 dSphs with DEIMOS in the fall seasons of 2015, 2016, and 2017. We used one slitmask on each of the three more massive dSphs (And VII, I, and III). We used two slitmasks in each of the two less

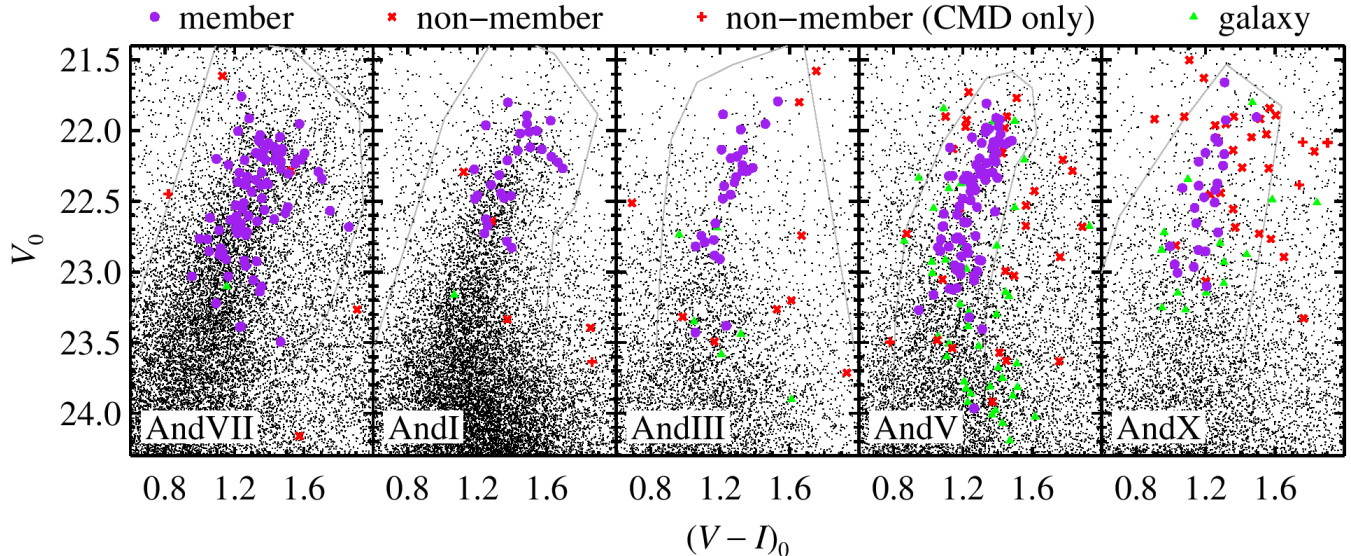


Figure 1. CMDs of the M31 dSphs. Colored points show DEIMOS spectroscopic targets. Purple circles show spectroscopically confirmed member stars, as described in Section 2.5. Red \times 's indicate stars with a spectroscopic disqualifier for membership (radial velocity or a strong Na I doublet). Stars ruled as non-members on the basis of CMD position alone are represented by red + signs. Unresolved galaxies are shown as green triangles. The many small black points indicate objects without spectra. Section 2.1 describes the spectroscopic target selection. The gray polygons define the boundaries of the CMD membership criterion, discussed in Section 2.5.

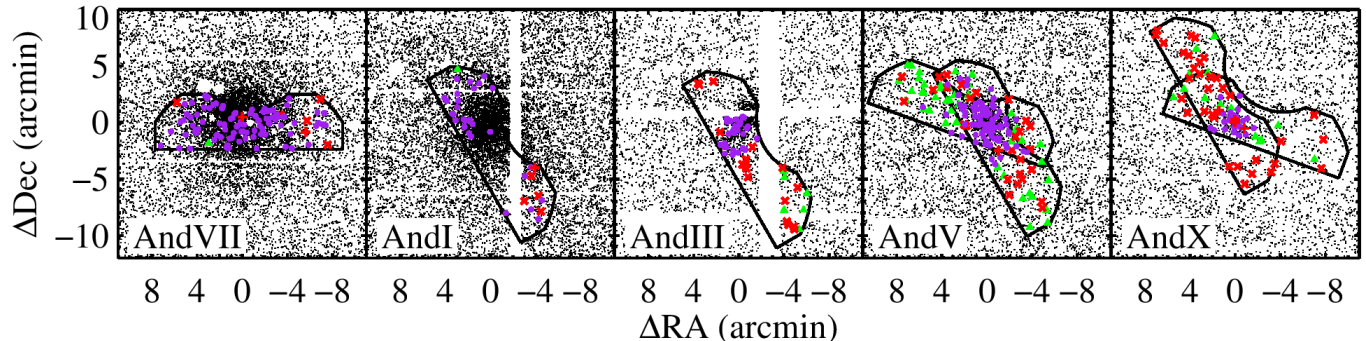


Figure 2. Maps showing the positions and orientations of the DEIMOS slitmasks. The irregular shapes delineate DEIMOS's field of view. Coordinates are relative to the galaxy centers (Tollerud et al. 2012). Symbols and colors have the same meaning as in Figure 1. Section 2.1 describes the slitmask design.

massive dSphs (And V and X) because their lower stellar density made for sparser sampling on each slitmask. Using two slitmasks allowed us to increase the sample sizes.

The observations were conducted with the 1200G grating at a central wavelength of 7800 Å. This configuration provides a spectral range of approximately 6300–9100 Å, but the range varies depending on the location of the slit on the slitmask. We used 0.7'' slits, which yielded a spectral resolution of approximately 1.2 Å FWHM. The resolution was a slight function of wavelength due to changes in anamorphic demagnification and image quality along the direction of dispersion. We aligned the slitmasks using at least four bright alignment stars that

were centered in 4'' boxes. The position angles of the slits were the same for all slits on a given slitmask, and that angle was chosen to be close to the parallactic angle at the expected time of observation. This choice minimized slit losses due to differential atmospheric refraction. Afternoon exposures of an internal quartz lamp were used for flat fielding, and afternoon exposures of Ne, Ar, Kr, and Xe arc lamps (turned on simultaneously) provided wavelength calibration. DEIMOS's active flexure compensation system minimized shifts of the image on the detector due to the changing gravity vector during the observations.

Table 1 gives the exposure times for each slitmask, separated by date of observation. The table also gives

Table 1. DEIMOS Observations

Galaxy	Slitmask	Slits	Tot. Exp. Time (hr)	Exp. Time (min)	Exposures per visit	Seeing (")	UT Date
Andromeda VII	and7a	119	4.6	71	3	0.9	2016 Sep 25
				53	3	0.8	2016 Sep 26
				80	3	0.9	2016 Sep 27
				72	3	1.1	2017 Jan 1
Andromeda I	and1a	98	5.1	69	3	0.8	2015 Oct 8
				66	3	0.8	2015 Oct 9
				20	3	0.8	2016 Sep 25
				30	1	0.9	2016 Sep 26
				120	4	0.5	2016 Dec 29
Andromeda III	and3a	75	5.3	175	7	1.0	2015 Oct 8
				143	6	0.7	2016 Sep 7
Andromeda V	and5a	107	6.7	199	7	0.9	2015 Oct 7
				206	7	0.9	2016 Sep 27
	and5b	104	5.0	203	8	0.5	2016 Sep 7
Andromeda X	and10a	62	4.9	180	6	1.0	2015 Oct 9
				116	4	0.6	2016 Sep 28
	and10b	51	6.2	180	6	0.8	2016 Sep 28
				101	4	0.6	2016 Dec 28
				88	3	1.1	2017 Jan 1

the total number of slits for each slitmask. That number excludes alignment stars, but it includes dSph non-members and slits that yielded no useful spectra.

The raw spectra were reduced with the spec2d pipeline (Cooper et al. 2012; Newman et al. 2013). The pipeline traces the edges of each slit using the quartz lamp exposures. After excising the two-dimensional, spectrally dispersed image of the slit in each of the calibration and on-sky frames, the pipeline computed a flat field correction from the quartz lamp exposure. The pipeline traced the arc lines across the slit to provide a two-dimensional wavelength solution for the slit. The flat field was applied to the on-sky images. Images obtained within the same observing run were coadded into a single image of the slit. Then, the spectrum of the object was extracted in a boxcar window.

The heliocentric correction can change by up to 0.4 km s^{-1} per day in the direction of M31. Furthermore, the reference frame for flexure compensation in DEIMOS drifts from night to night. It is difficult to maintain the same reference frame for more than a week. For these reasons, we limited two-dimensional coaddition to images taken within the same observing run. The observing runs spanned no more than 3 nights in September, when the heliocentric correction

changes the most from night to night, and 5 nights in December/January, when the heliocentric correction changes by only 0.1 km s^{-1} per night. We extracted one-dimensional spectra from each of these subsets. Then, we coadded the one-dimensional spectra in the heliocentric frame using inverse variance weighting. The resulting spectrum is called s_{helio} . We also made a separate version of the coaddition in the geocentric frame. The resulting spectrum (s_{geo}) was used to determine the slit centering correction (Section 2.3).

Some stars in And V and And X were observed on two separate slitmasks. Their one-dimensional spectra were coadded in the same manner described in the previous paragraph. The total exposure times for these stars were 11.7 hours (And V) and 11.1 hours (And X).

We estimated the signal-to-noise ratio (SNR) for each spectrum with the following procedure. We calculated the absolute deviation from 1 of the continuum-normalized spectra in the “continuum regions” defined by Kirby et al. (2008). These regions are defined from a the model spectrum of a star with $T_{\text{eff}} = 4300 \text{ K}$, $\log g = 1.5$, and $[\text{Fe}/\text{H}] = -1.5$. The continuum regions are contiguous spectral windows with widths of at least 0.5 \AA . In order to qualify as a continuum region, every pixel in the window must have a flux decrement less

than 4% when smoothed to the spectral resolution of DEIMOS’s 1200G diffraction grating. Within the continuum regions, we discarded pixels that exceeded three times the median deviation in order to discount pixels still affected by absorption lines in the star. The SNR was defined as the inverse of the median deviation of the remaining pixels. The SNR of our sample ranges from 4 \AA^{-1} to 73 \AA^{-1} with a median of 21 \AA^{-1} . To convert to SNR per pixel, the SNR per \AA can be multiplied by $\sqrt{0.33}$, where 0.33 is the number of \AA per pixel.

Figure 3 shows some example spectra at the extremes of metallicity and SNR. The spectra are shown in only a small region of the full wavelength range. Although the figure shows the best-fitting synthetic spectra, the majority of the abundance information falls outside of this spectral range. In particular, the Ca II triplet shown in Figure 3 is not used to measure abundances, but it is used to measure radial velocities.

2.3. Velocity Measurements

We measured radial velocities using the procedures previously described by Kirby et al. (2015), who based their method on that of Simon & Geha (2007). We summarize the method here.

We measured velocities by cross-correlating the one-dimensional spectrum (s_{helio}) with template spectra observed with DEIMOS by Kirby et al. (2015). Nine radial velocity standard stars (mostly metal-poor giants) comprise the template library. The velocities are determined by minimizing χ^2 between the target and template spectra while the redshift of the target spectrum was varied. The entire spectrum except for regions of strong telluric absorption was used in the cross correlation. All of the velocity measurements were confirmed by visual inspection. In some cases, the automated cross correlation failed, often because incompletely subtracted sky emission lines affected the measurement. In these cases, the velocity was re-measured with a wavelength range restricted approximately to the Ca II triplet (8450–8700 \AA in the observer frame).

The velocity measurements can be affected by the position of the star in the slit. If the center of the star is misaligned perpendicular to the slit (along the dispersion axis), then the stellar spectrum will have a different wavelength zeropoint than the arc line spectrum. The reason is that the arc lines completely fill the slit, whereas the stellar spectrum has a peaked profile that does not fill the slit uniformly. We corrected the wavelength zeropoint by calculating the apparent velocity shift of telluric absorption features in the spectrum (see Sohn et al. 2007). Because the telluric features are absorbed from the starlight, they have the same zeropoint as the starlight. We measured the “velocity” of the telluric features using the same cross correlation method described in the previous paragraph. We used the spectrum coadded in the geocentric frame (s_{geo}) rather than the heliocentric frame because the tel-

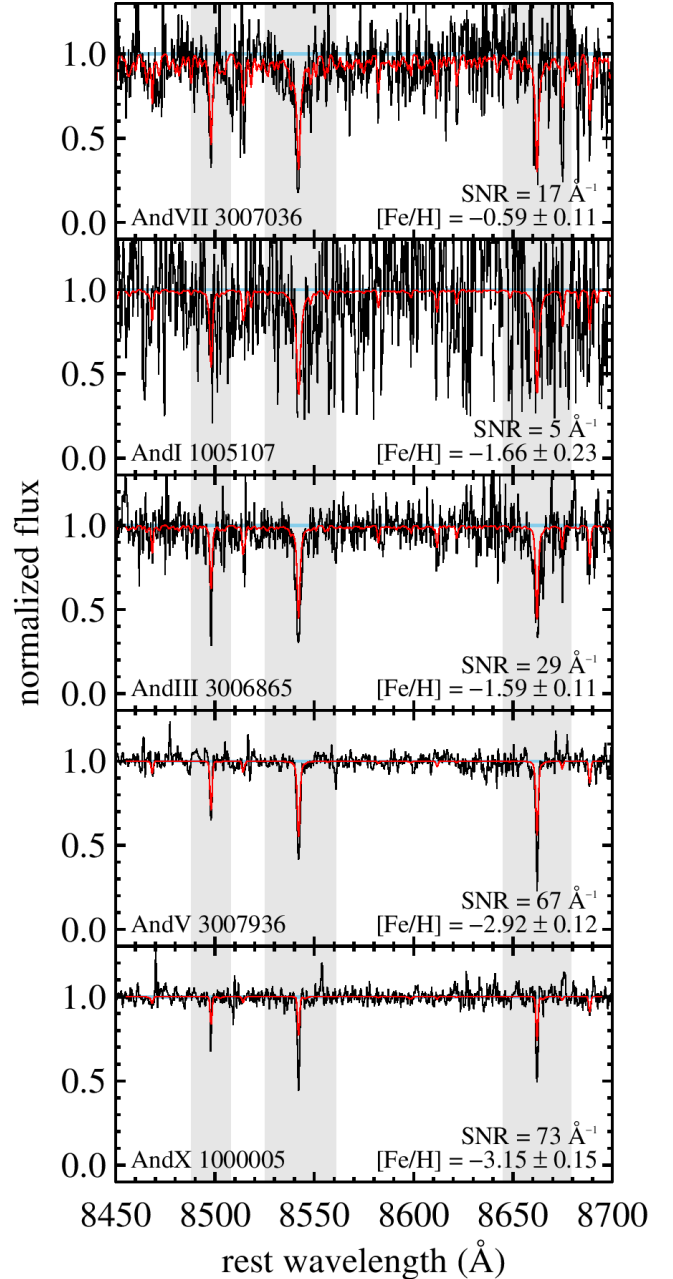


Figure 3. Portions of example DEIMOS spectra in each M31 dSph. The spectra shown are the star with the highest $[\text{Fe}/\text{H}]$ in And VII, the spectrum in And I with the lowest SNR that still permitted a measurement of $[\text{Fe}/\text{H}]$, the spectrum in And III with the median SNR, the spectrum in And V with the highest SNR, and the spectrum in And X with the lowest $[\text{Fe}/\text{H}]$. The red curve shows the best-fitting synthetic spectrum. The Ca II triplet (gray shading) is not well modeled and excluded from the abundance determination. The full wavelength range is approximately 6300–9100 \AA .

luric features should be at rest in the geocentric frame, and the transformation from geocentric to heliocentric frames varies across the observations. We cross correlated this spectrum with the template spectrum of a hot star, also observed by Kirby et al. (2015). The wavelength range of the cross correlation was restricted to the regions of strong telluric absorption (6866–6912 Å, 7167–7320 Å, 7593–7690 Å, and 8110–8320 Å), which include the Fraunhofer A and B bands. The telluric correction was subtracted from the stellar radial velocity determined above to determine the final heliocentric velocity.

Our determinations of the slit centering correction were based on spectra coadded from multiple nights. In principle, the position of the star in the slit could change from night to night. Therefore, it would be best if we could measure the slit centering correction for each night of observation. However, the SNR from a single night is generally too low for a reliable measurement. Fortunately, the majority of the mis-centering results from astrometric errors. We used alignment stars with coordinates in the same astrometric system as the target stars. However, relative astrometric errors between the alignment and target stars will lead to slit mis-centering that is fairly constant from night to night. Proper motions could also cause the bright (presumably nearby, compared to M31) alignment stars to drift from the time their positions were measured. These errors are not necessarily constant in time, but they are confined to the small angular distance the stars moved in ~ 1 year, which is the approximate length of time between the first and last observations of any particular slitmask.

We estimated errors on the velocity through Monte Carlo sampling. We resampled the flux of each pixel from a Gaussian with a width corresponding to the square root of the variance estimated from the data reduction pipeline. We then recomputed the heliocentric velocity and its telluric correction. The random velocity error was taken to be the standard deviation of 10^3 samples.

The error also has a systematic component. Kirby et al. (2015) determined that the systematic error is 1.49 km s^{-1} from repeat measurements of the same stars. The final velocity error is equal to the random error added in quadrature with the systematic error.

2.4. Abundance Measurements

We measured elemental abundances using spectral synthesis in local thermodynamic equilibrium (LTE) in the same manner as Kirby et al. (2008, 2009, 2010). This section gives a summary of the procedure.

We prepared the observed spectra for abundance measurement by telluric correction, shifting to the rest frame, and continuum normalization. We constructed a telluric absorption template from the continuum-normalized spectrum of a hot star. This spectrum was raised to the ratio of the airmasses of the target star and

the hot star in order to account for different amounts of atmospheric absorption between the telluric and target spectra. Then, the target star’s spectrum was divided by this scaled telluric spectrum. Next, the spectrum was shifted into the rest frame according to the velocity determined in Section 2.3. Finally, we made an initial attempt at determining the continuum. We fit a spline to the “continuum regions” defined by Kirby et al. (2008). The spline had a breakpoint spacing of 100 pixels. The spectrum was divided by the spline.

We then searched for the best-fitting synthetic spectrum among a grid of synthetic spectra (Kirby 2011). The spectra were computed with MOOG (Sneden 1973; Sneden et al. 2012) coupled with ATLAS9 (Kurucz 1993) model atmospheres and Kirby et al.’s (2008) line list. We searched the grid in effective temperature (T_{eff}) and metallicity ($[\text{Fe}/\text{H}]$) using the MPFIT implementation (Markwardt 2012) of Levenberg–Marquardt χ^2 minimization. The surface gravity ($\log g$) was fixed at the photometric isochrone value assuming distance moduli of $m - M = 24.51$ for And I, 24.38 for And III (Skillman et al. 2017), 24.44 for And V, 24.41 for And VII (McConnachie et al. 2005), and 24.26 for And X (Weisz et al. 2019). The spectral range for calculating χ^2 was restricted to regions immediately surrounding iron and α element absorption lines. After T_{eff} and $[\text{Fe}/\text{H}]$ were determined, we searched the grid again, this time restricting the spectral range to α element absorption lines and varying only $[\alpha/\text{Fe}]$. The value of $[\alpha/\text{Fe}]$ was used for both the ATLAS9 model atmosphere and the MOOG synthesis.

We then refined the determination of the continuum. A synthetic spectrum was constructed from the initial measurements of T_{eff} , $\log g$, $[\text{Fe}/\text{H}]$, and $[\alpha/\text{Fe}]$. The observed spectrum was divided by this synthetic spectrum, and a spline with a breakpoint spacing of 150 pixels was fit to the quotient. The spline was fit to the entire spectrum excluding regions of strong telluric absorption and some strong absorption lines that were not well modeled, including $\text{H}\alpha$ and the Ca II triplet.² We divided the observed spectrum by this spline and repeated the measurements of T_{eff} , $[\text{Fe}/\text{H}]$, and $[\alpha/\text{Fe}]$. This procedure was iterated until T_{eff} changed by less than 1 K and $[\text{Fe}/\text{H}]$ and $[\alpha/\text{Fe}]$ each changed by less than 0.001 dex.

We then measured individual elemental abundances. We made a final measurement of $[\text{Fe}/\text{H}]$ by fixing T_{eff} and $[\alpha/\text{Fe}]$ and then performing a grid search restricted

² The core of each line in the Ca II triplet forms high in the photosphere or chromosphere, where the LTE assumption may not be valid. For most stars, the majority of the triplet’s equivalent width comes from the damping wings. Therefore the abundance depends strongly on how well the damping constants are known. For these reasons, abundances measured with the triplet are usually based on scaling relations, which are either empirical (e.g., Rutledge et al. 1997; Battaglia et al. 2008b) or based on non-LTE modeling (Starkenburg et al. 2010). We exclude the triplet because our synthetic spectra assume LTE.

only to Fe absorption lines. Abundances of Mg, Si, Ca, and Ti were measured in a similar manner. We used the same model atmosphere for all of the individual abundance measurements. That means that the value of $[\alpha/\text{Fe}]$ used to pick the ATLAS9 model atmosphere was fixed at the value determined after the last step of the continuum iteration. The individual abundances were determined by varying their values within MOOG.

When we refer to $[\alpha/\text{Fe}]$, we mean the value of $[\alpha/\text{Fe}]$ used in the model atmosphere to determine all of the individual abundances. This value is informed by a combination of Mg, Si, Ca, and Ti lines. We separately refer to the individual element ratios as $[\text{Fe}/\text{H}]$, $[\text{Mg}/\text{Fe}]$, $[\text{Si}/\text{Fe}]$, $[\text{Ca}/\text{Fe}]$, and $[\text{Ti}/\text{Fe}]$.

V14a measured $[\text{Fe}/\text{H}]$ and $[\alpha/\text{Fe}]$ for many of the stars in our sample. They used shallower DEIMOS spectroscopy. The advantage of our sample is the higher SNRs of individual spectra, which result in more precise abundance measurements and the ability to measure individual element ratios. Appendix A contains a comparison of our measurements with those of V14a.

2.5. Membership

We could not always fill the slitmask with candidate member stars. Therefore, we designed the slitmasks to include more targets than we expected to be members of the dSphs. In some cases, simply to fill available space for slits, we included targets that we knew in advance to be non-members on the basis of their positions in the CMD. In addition to CMD position, we also considered the strength of the Na I doublet at 8190 Å and radial velocity as membership criteria.

The spectra revealed some objects to be galaxies rather than individual stars. The majority of these galaxies were identified by the presence of redshifted emission lines, such as [O II] at 3727 Å in the rest frame. There were also two absorption-line galaxies in the direction of And X whose spectra showed redshifted Ca H and K in absorption.

We selected dSph members on the basis of their CMD positions by drawing a wide region around the corresponding RGB tailored for each dSph (gray polygons in Figure 1). The boundaries of the region were subjective, but the region was chosen to be as inclusive as reasonable to avoid a color (i.e., metallicity) bias in the target selection. The large majority of stars rejected on the basis of CMD position were also rejected for at least one other reason. A total of 8 stars across all dSphs were rejected on the basis of their CMD position alone. These stars are bluer, redder, or brighter than the RGB in the relevant dSph.

The Na I doublet at 8190 Å is sensitive to surface gravity. It is strong in dwarf stars and weak in giants. As a result, the presence of a strong doublet would indicate that the star is a foreground dwarf rather than a giant at the distance of M31. Kirby et al. (2012) found that a summed equivalent width exceeding 1 Å indicated a sur-

face gravity in excess of $\log g = 4.5$. Such an equivalent width is easily visible by eye in our spectra, and it is accompanied by strong damping wings. We inspected all spectra visually. Stars displaying a strong Na I doublet were flagged as non-members. The Mg I line at 8807 Å is also a good surface gravity diagnostic (Battaglia & Starkenburg 2012), but we do not use it because some of our spectra do not reach that wavelength, and the line is usually weaker than the Na I doublet.

We also used radial velocity as a membership criterion. Section 3.1 describes our procedure for determining the mean velocity and velocity dispersion (σ_v) of each dSph. Any star more than $3\sigma_v$ from the mean velocity was considered a non-member.

Table 2 presents the coordinates, extinction-corrected magnitudes, SNR, velocity, elemental abundances, and membership information for each observed star. Stars observed on two slitmasks are identified with the letters “ab.” For example, “and5ab” means that the star was observed on the slitmasks and5a and and5b. Only abundances with errors less than 0.4 dex are given. The last column of the table gives comments for some stars as well as reasons for excluding a star from membership consideration. The codes “CMD,” “v,” and “Na” mean that a star was ruled a non-member because of its CMD position, velocity, or Na I doublet strength, respectively. Many stars have multiple codes because they displayed multiple non-membership traits. The code “G” means that the object is a galaxy, not a star. Stars are also marked for displaying CN or C₂ absorption (“C”) or TiO absorption (“TiO”), although these were not considered in the determination of membership. Although our synthetic spectra do have CN and C₂ features, they lack TiO. For this reason, Gilbert et al. (2019) and Escala et al. (2019a,b) treated TiO stars as a special case. However, only one star in our sample (And VII 3009310) has both TiO absorption and a measurement of $[\text{Fe}/\text{H}]$. Therefore, we do not consider TiO a significant source of bias in our sample.

3. KINEMATICS

In this section, we quantify the dynamical masses of five M31 dSphs and examine their constituent members for evidence of rotation. Unfortunately, the sample sizes are insufficient to test for kinematic substructure, such as multiple chemodynamical populations (e.g. Walker & Peñarrubia 2011). Sample sizes of at least several hundreds are required for this purpose (e.g., Battaglia et al. 2008a; Amorisco & Evans 2012; Pace et al. 2014).

3.1. Velocity Dispersion and Mass

Figure 4 shows the velocity distributions for each galaxy. Each dSph shows an obvious peak in radial velocity. It is also apparent that the velocity dispersion (σ_v) is the highest for the dSph with the highest stellar mass (And VII) and lowest for the dSph with the lowest stellar mass (And X).

Table 2. Catalog of Abundances

DSph	Star ID	RA (J2000)	Dec (J2000)	V_0 (mag)	I_0 (mag)	Slitmask	S/N	v_{helio} (km s ⁻¹)
And VII	7000796	23:25:44.96	+50:40:17.7	23.06 ± 0.06	21.75 ± 0.04	and7a	5.2	-343.31 ± 4.81
And VII	7000745	23:25:45.78	+50:41:22.9	22.43 ± 0.04	21.13 ± 0.03	and7a	10.7	-313.66 ± 3.52
And VII	7000663	23:25:46.72	+50:40:22.3	23.10 ± 0.07	21.75 ± 0.04	and7a	5.0	-303.05 ± 12.77
And VII	7000436	23:25:49.01	+50:40:30.4	22.86 ± 0.05	21.73 ± 0.03	and7a	7.0	-309.94 ± 7.08
And VII	7000338	23:25:49.62	+50:41:26.2	22.56 ± 0.04	21.19 ± 0.02	and7a	9.7	-309.78 ± 5.11
And VII	7000349	23:25:50.32	+50:40:15.5	22.30 ± 0.03	21.07 ± 0.02	and7a	12.1	-297.95 ± 3.73
And VII	3013816	23:25:54.65	+50:38:34.9	22.63 ± 0.05	21.20 ± 0.02	and7a	13.8	-321.66 ± 2.92
And VII	3013989	23:26:02.55	+50:40:30.0	22.23 ± 0.04	20.68 ± 0.02	and7a	18.3	-328.35 ± 3.12
And VII	3012195	23:26:03.95	+50:38:16.1	22.21 ± 0.03	20.77 ± 0.02	and7a	22.5	-321.78 ± 2.55
And VII	3013609	23:26:04.89	+50:39:32.7	22.10 ± 0.03	20.72 ± 0.02	and7a	25.4	-297.24 ± 2.10

Member?	T_{eff} (K)	log g (cm s ⁻²)	[Fe/H]	[α /Fe]	[Mg/Fe]	[Si/Fe]	[Ca/Fe]	[Ti/Fe]	Comment
Y	4258 ± 51	1.10	-1.62 ± 0.30	
Y	4277 ± 50	0.86	-2.17 ± 0.23	
Y	4187 ± 54	1.07	-1.46 ± 0.25	
Y	
Y	4181 ± 40	0.83	-2.35 ± 0.29	
Y	4413 ± 39	0.90	-2.13 ± 0.23	+0.64 ± 0.37	
Y	4125 ± 32	0.80	-1.43 ± 0.13	
Y	3991 ± 22	0.51	-1.84 ± 0.13	+0.22 ± 0.25	+0.08 ± 0.21	
Y	4113 ± 22	0.62	-1.85 ± 0.13	+0.72 ± 0.18	+0.70 ± 0.18	
Y	4201 ± 23	0.64	-1.59 ± 0.11	-0.04 ± 0.21	-0.05 ± 0.20	

NOTE—(This table is available in its entirety in machine-readable form.)

We measured the mean velocity ($\langle v_{\text{helio}} \rangle$) and σ_v for each dSph using maximum likelihood. We closely followed the procedure of Walker et al. (2006). The likelihood function is

$$L = \prod_i \frac{1}{\sqrt{2\pi(\sigma_v^2 + \delta v_{\text{helio},i}^2)}} \exp \frac{-(v_{\text{helio},i} - \langle v_{\text{helio}} \rangle)^2}{2(\sigma_v^2 + \delta v_{\text{helio},i}^2)} \quad (1)$$

The product operates over all member stars i . The heliocentric velocity of star i is $v_{\text{helio},i}$, and its uncertainty is $\delta v_{\text{helio},i}$. The free parameters are $\langle v_{\text{helio}} \rangle$ and σ_v .

We found the maximum likelihood with a Monte Carlo Markov chain (MCMC) using a Metropolis algorithm. We adopted the initial values of $\langle v_{\text{helio}} \rangle$ and σ_v from Tollerud et al. (2012), who measured the kinematics of M31 satellites from shallower DEIMOS spectra. The proposal density of the Metropolis algorithm was a nor-

mal distribution with $\sigma = 2.5$ km s⁻¹. The chain had 10⁶ links plus an initial 10⁵ links, which were discarded as burn-in. Visual inspection of the chains showed that they were well-converged after burn-in. We took the most likely values of $\langle v_{\text{helio}} \rangle$ and σ_v to be the medians (50th percentile) of the distributions. The asymmetric 1 σ errors are those values that enclose 68% of the distribution (16th and 84th percentiles).

Our first attempt at measuring these values included stars whose velocities satisfied the criterion $|v_{\text{helio},i} - \langle v_{\text{helio}} \rangle| < 3\sigma_v$, using the $\langle v_{\text{helio}} \rangle$ measurements of Tollerud et al. (2012) as a starting guess. After computing new measurements of $\langle v_{\text{helio}} \rangle$ and σ_v , we re-evaluated the membership of each star using the $3\sigma_v$ criterion. Then, we recomputed the entire MCMC chain. We iterated this procedure until the list of member stars was unchanged between iterations.

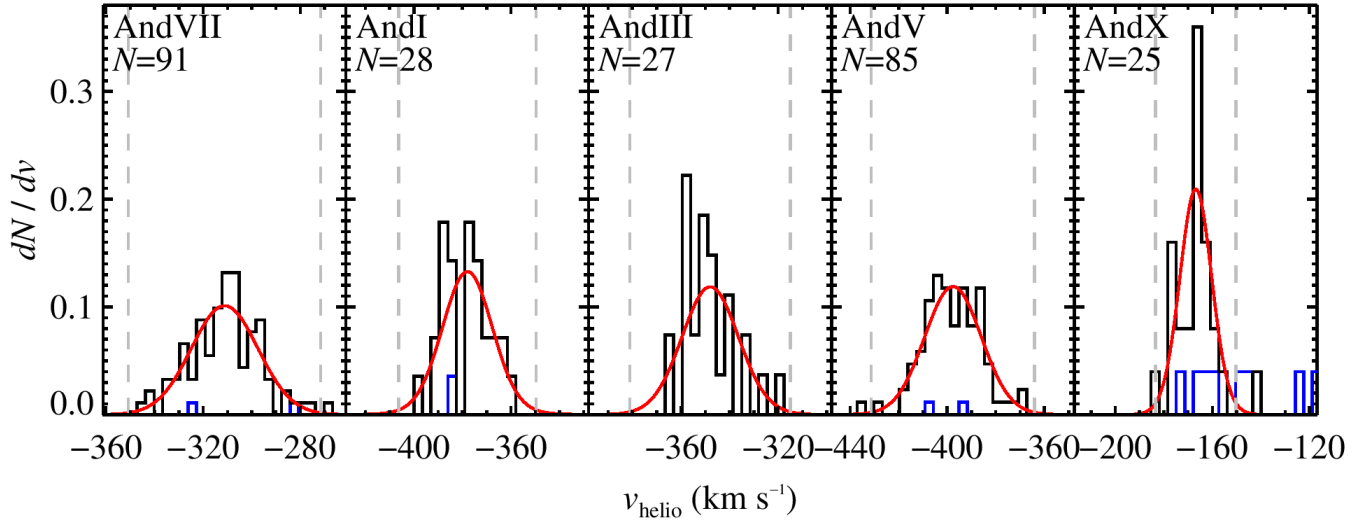


Figure 4. Histograms of heliocentric radial velocities of individual stars in each dSph. Stars that fail any membership criterion other than radial velocity are represented by the blue histograms. The black histograms show the remaining potential members. The histograms are normalized to enclose the same area in each panel regardless of the number of measurements. The red curves show Gaussians with the measured σ_v for each galaxy. The curves are convolved with a function to approximate the widening induced by observational uncertainty. This function is the sum of N equal-area Gaussians, where N is the number of stars in the histogram. The width, σ_i , of each Gaussian is the measurement uncertainty of star i . The dashed gray vertical lines show the bounds of the velocity membership criterion. Each panel gives the number of members (N) in the dSph. Section 2.3 describes the radial velocity measurements, and Section 3.1 describes how we quantify the resulting velocity distributions.

Table 3. Kinematical Properties of M31 dSphs

DSph	M_*/L_V^a	$\log M_*^b$	N_{mem}	$\langle v_{\text{helio}} \rangle$	σ_v	$r_{1/2}^c$	$\log M_{1/2}$	$(M/L)_{1/2}^d$	$ v_{\text{rot}} ^e$
	(M_\odot/L_\odot)	(M_\odot)		(km s^{-1})	(km s^{-1})	(pc)	(M_\odot)	(M_\odot/L_\odot)	(km s^{-1})
And VII	0.9	7.21 ± 0.12	91	-311.2 ± 1.7	$13.2^{+1.2}_{-1.1}$	980 ± 50	8.08 ± 0.08	13 ± 4	< 7.9
And I	1.6	6.86 ± 0.40	28	$-378.0^{+2.4}_{-2.3}$	$9.4^{+1.7}_{-1.5}$	830 ± 40	$7.71^{+0.16}_{-0.14}$	23 ± 22	< 9.0
And III	1.8	6.27 ± 0.12	27	$-348.0^{+2.7}_{-2.6}$	$11.0^{+1.9}_{-1.6}$	520	$7.65^{+0.15}_{-0.13}$	86^{+38}_{-34}	< 9.5
And V	1.1	5.81 ± 0.12	85	-397.7 ± 1.5	$11.2^{+1.1}_{-1.0}$	450 ± 20	7.59 ± 0.08	132^{+44}_{-43}	< 6.1
And X	1.6^f	5.08 ± 0.03	25	-166.9 ± 1.6	$5.5^{+1.4}_{-1.2}$	310 ± 30	$6.82^{+0.22}_{-0.20}$	177^{+92}_{-81}	< 5.5

^aStellar mass-to-light ratio measured by Woo et al. (2008).

^bStellar mass, calculated from the product of luminosity measured by Tollerud et al. (2012) and stellar mass-to-light ratio from the previous column.

^c3-D de-projected half-light radius, taken from Tollerud et al. (2012).

^dDynamical mass-to-light ratio within the half-light radius, where the luminosity is taken from Tollerud et al. (2012).

^e98% confidence level upper limit.

^fWoo et al. (2008) did not calculate M_*/L for And X. We assume the average value for dSphs measured by Woo et al. (2008).

Table 3 gives summary structural and kinematical information for stars in the dSphs. It is worth discussing the stellar mass measurements because so many properties of the dSphs depend on stellar mass. We adopt the M_* measurements of [Woo et al. \(2008\)](#). That study estimated stellar mass in two different ways: scaling relations between integrated galaxy colors and M_*/L ([Bell & de Jong 2001](#)) and integrations of SFHs from CMDs ([Mateo 1998](#)). Although [Woo et al.](#) did not calculate uncertainties on M_*/L for each galaxy, we can estimate the uncertainties by the scatter between the two mass measurement methods. The standard deviation of the difference in mass measurements is 0.16 dex (a factor of 1.5). The deviations do not depend on galaxy luminosity. [Woo et al.](#) used the SFH method for the two M31 dSphs (And I and And III) for which they had access to measured SFHs. They used the color–mass relation for And V and And VII. They did not have any measurements for And X, which was discovered just prior to the publication of their paper. Therefore, we assume that And X has the average value of M_*/L for the dSphs that [Woo et al.](#) included in their sample.

The values for $\langle v_{\text{helio}} \rangle$ and σ_v are largely consistent with previous measurements ([Tollerud et al. 2012](#); [Collins et al. 2013](#)).³ The most discrepant measurement is $\langle v_{\text{helio}} \rangle$ for And VII, for which our measurement differs by 2.3 standard deviations from that of [Tollerud et al. \(2012\)](#). The average offset in $\langle v_{\text{helio}} \rangle$ is 2.5 km s^{-1} , where our measurements are more negative. The offset is probably a result of a difference in velocity zeropoints between the radial velocity template spectra. If we shift all of our measurements of $\langle v_{\text{helio}} \rangle$ by 2.5 km s^{-1} , they agree with [Tollerud et al. \(2012\)](#) within 1.1 standard deviations. All of the measurements of σ_v are consistent within one standard deviation.

The dynamical mass of each dSph can be estimated using the formula of [Wolf et al. \(2010\)](#): $M_{1/2} = 3G^{-1}\sigma_v^2 r_{1/2}$, where $r_{1/2}$ is the 3-D (de-projected) half-light radius, $M_{1/2}$ is the mass enclosed within $r_{1/2}$, and G is the gravitational constant. We adopt the values of $r_{1/2}$ from [Tollerud et al. \(2012\)](#). These values agree with those of [Martin et al. \(2016\)](#) except for And I, where [Martin et al.](#)’s measurement is larger by 31% after correcting for de-projection. The value of $M_{1/2}$ would be larger by the same factor if we used the larger half-light radius. Our measurements of $M_{1/2}$, shown in Table 3, are entirely consistent with those of [Tollerud et al. \(2012\)](#), which is not surprising given that measurements of σ_v are consistent.

These mass estimates reaffirm that the dSph satellites of M31 are dominated by dark matter. The dynamical mass-to-light ratios ($M/L = 2M_{1/2}/L$) are given in Ta-

ble 3. In agreement with previous studies, the values are in excess of what would be expected ($M/L \sim 2$) for an ancient stellar population in dynamical equilibrium with no dark matter. The ratios of total mass to stellar mass within the half-light radii ($2M_{1/2}/M_*$) range from 14_{-9}^{+24} (And I) to 120_{-34}^{+48} (And V). The ratio for a dSph devoid of dark matter would be ~ 1 .

Stars in binary systems exhibit radial velocity variability, which inflates measurements of σ_v . The effect is to spuriously increase mass estimates because the increase in σ_v does not reflect the depth of the galaxy’s gravitational potential. The best practice is to identify stars with variable velocities via multiple epochs of spectroscopy. In principle, we could have used previous SPLASH observations and subsets of our own observations to quantify binarity. However, binarity negligibly affects σ_v for galaxies with $\sigma_v \sim 10 \text{ km s}^{-1}$ ([Spencer et al. 2017](#)). [Minor et al. \(2010\)](#) also showed that binarity does not significantly affect mass estimates of classical dSphs.

3.2. Rotation

dSphs generally do not exhibit rotation. [Wheeler et al. \(2017\)](#) found that dSphs generally have rotation-to-dispersion ratios of $v_{\text{rot}}/\sigma_v < 0.5$. And II, one of M31’s dSph satellites, is a notable exception. It not only rotates, but it rotates at 8.6 km s^{-1} about its major axis, i.e., prolate rotation ([Ho et al. 2012](#)). The ratio of rotation to dispersion is $v_{\text{rot}}/\sigma_v = 1.1 \pm 0.3$. This unusual sense of rotation has been suggested to reflect a merger of two dwarf galaxies of similar mass ([Amorisco et al. 2014](#); [Lokas et al. 2014](#); [Fouquet et al. 2017](#)). In light of the information that rotation possibly encodes, we tested for and quantified rotation in the five M31 satellites in our sample.

We followed [Wheeler et al.](#)’s (2017) procedure for measuring rotation. The method is an extension of the measurement of σ_v presented in Section 3.1. Introducing rotation requires a slight modification of the likelihood function.

$$L = \prod_i \frac{1}{\sqrt{2\pi(\sigma_v^2 + \delta v_{\text{helio},i}^2)}} \exp \frac{-(v_{\text{helio},i} - v'_i)^2}{2(\sigma_v^2 + \delta v_{\text{helio},i}^2)} \quad (2)$$

$$v'_i = \langle v_{\text{helio}} \rangle + v_{\text{rot}} \cos(\theta - \theta_i) \quad (3)$$

Equation 3 represents a flat rotation curve with a velocity of v_{rot} relative to $\langle v_{\text{helio}} \rangle$. Star i has a position angle of θ_i measured with respect to the center of the dSph (coordinates taken from [Tollerud et al. 2012](#)). The angle θ is the orientation of the rotation axis. The velocity v_{rot} is unconstrained, but θ is constrained between 0° and 180° . [Wheeler et al.](#) also considered an isothermal model of rotation, but we chose to keep our test for rotation as simple as possible. The isothermal model might be more realistic than the flat rotation curve, but it also

³ Our sample sizes are smaller than those of [Tollerud et al. \(2012\)](#) but larger than that of [Collins et al. \(2013\)](#). Our exposure times are longer than both studies by a factor of 5–10.

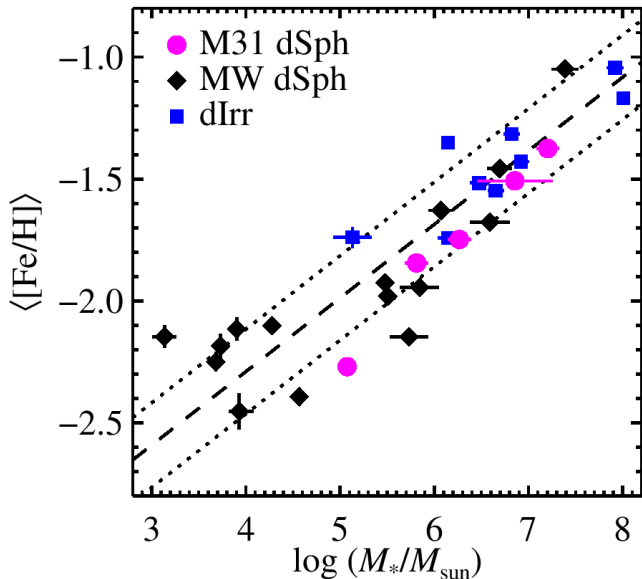


Figure 5. Stellar mass–metallicity relation of Local Group dwarf galaxies. The M31 dSphs are those analyzed in this paper. The MW dSphs and Local Group dIrrs were analyzed by K13. The dotted line shows the MZR fit to dIrrs and MW dSphs (K13), and the dotted lines show the 1σ dispersion. The M31 dSphs follow the relation. Whereas the K13’s version of this plot relied on coadded spectra for M31 dSphs, this plot is based entirely on metallicity measurements for individual stars. Section 2.4 provides an overview of the abundance measurements, and Section 4 discusses the implications of the measurements.

benefits from a large sample out to large radius, which our sample does not provide.

We found the posterior distributions of $\langle v_{\text{helio}} \rangle$, σ_v , v_{rot} , and θ using the same MCMC procedure described in Section 3.1. In all cases, the inner 68% of the posterior distribution of v_{rot} includes zero. The $|v_{\text{rot}}|$ upper limits that include 95% of all MCMC trials for the five dSphs range from 6 to 10 km s $^{-1}$ (see Table 3). Thus, we found no evidence for rotation in these galaxies, consistent with previous studies using shallower spectroscopy. These non-detections reinforce that And II is especially unusual for exhibiting not only rotation but prolate rotation.

4. METALLICITY

In this section, we analyze the stellar metallicities of the M31 dSphs. First, we discuss the MZR of the M31 satellites. Then, we interpret the MDFs through the lens of one-zone models of chemical evolution. We include a comparison of the M31 dSph MDFs with those of MW dSphs.

4.1. Metallicity Distributions

Table 4 and Figure 5 show the average stellar metallicities⁴ of our five M31 dSphs. The error bars for $\langle [Fe/H] \rangle$ reflect the error on the mean. Table 4 also gives the inverse variance-weighted standard deviation and median of each MDF. The mean differs from the median both because the MDFs are asymmetric and because the mean is weighted by inverse variance, whereas the median is not.

The metallicities increase monotonically with stellar mass, in line with the well-established MZR. Furthermore, the MZR of M31 dSphs lies within the envelope defined by MW dSphs (K13). And X’s metallicity lies outside of the 1σ dispersion, but it is well in line with low-mass MW satellites. It falls directly between those of Ursa Minor and Hercules. All of the M31 dSphs fall slightly below the best-fit relation measured by K13 but no more so than some of the MW dSphs.

K13 and V14a previously measured the average metallicities of all five dSphs in our sample. K13 used spectral coaddition rather than measurements of individual stars. Despite the difference in technique, our new measurements agree within 0.2 dex except for And VII, which we find to be 0.25 dex more metal-rich than K13. V14a measured metallicities of individual stars, using nearly the same code that we use here. The major difference between the two studies is that the spectra analyzed here have higher SNR. Additionally, we adopt a slightly different membership selection here. Our measurements agree with those of V14a within 0.2 dex except for And I, which we measure to be 0.40 dex more metal-poor. The agreement is notable because we find an offset of $+0.30 \pm 0.02$ in $[Fe/H]$ between our two studies (see Appendix A). We do not correct this offset in comparing the mean metallicities. Ho et al. (2015) also presented metallicity distributions of luminous M31 satellites, including And VII, using the Ca II infrared triplet. They found $\langle [Fe/H] \rangle = -1.30 \pm 0.07$, in close agreement with our own measurement.

4.2. Chemical Evolution Models

A galaxy’s gas flow history shapes its MDF. Therefore, the MDF can be used as a tool to infer its past chemical evolution. The simplest way to consider galactic chemical evolution is a one-zone model (Pagel 1997). In this model, the galaxy’s gas is assumed to be well-mixed at all times. Therefore, it has a single composition at any time. The MDF shape is influenced by the yields of stellar populations (which are usually assumed to be constant with time), the flow of metals out of the galaxy, and the accretion of gas (usually assumed to be metal-free).

⁴ The quantity $\langle [Fe/H] \rangle$ is the average of the logarithmic stellar metallicities, $[Fe/H]$. As pointed out by Escala et al. (2018), many papers about galaxy simulations instead quote the logarithm of the average. The distinction should be kept in mind for any comparisons between observed and simulated galaxy metallicities.

Table 4. Chemical Properties of M31 dSphs

DSph	$N_{[\text{Fe}/\text{H}]}$	$\langle[\text{Fe}/\text{H}]\rangle$	$\sigma([\text{Fe}/\text{H}])$	median($[\text{Fe}/\text{H}]$)	$N_{[\alpha/\text{Fe}]}$	$\langle[\alpha/\text{Fe}]\rangle$
And VII	87	-1.37 ± 0.01	0.36	-1.39	56	$+0.18 \pm 0.03$
And I	28	-1.51 ± 0.02	0.34	-1.47	20	$+0.14 \pm 0.04$
And III	24	-1.75 ± 0.03	0.43	-1.98	21	$+0.11 \pm 0.04$
And V	81	-1.84 ± 0.01	0.41	-1.82	57	$+0.07 \pm 0.03$
And X	21	-2.27 ± 0.03	0.47	-2.38	9	$+0.27 \pm 0.09$

We fit the M31 dSph MDFs with the same models used by Kirby et al. (2011b) and K13. They are a Leaky Box Model (Schmidt 1963; Talbot & Arnett 1971), Pre-Enriched Model (Pagel 1997), and Accretion Model (Lynden-Bell 1975). The Leaky Box Model presumes that the galaxy can lose gas at a rate proportional to the SFR, but it does not acquire new gas. The only free parameter is the effective yield (p_{eff}), which is the stellar yield minus metal loss due to outflow. The Pre-Enriched Model that we use here is identical to the Leaky Box Model except that it has an additional free parameter: the initial metallicity ($[\text{Fe}/\text{H}]_0$). The Accretion Model is an extension of the Leaky Box Model where metal-free gas is allowed to fall onto the galaxy with a specific form as a function of time. The free parameters are p_{eff} and the accretion parameter M , which is the ratio of the final stellar mass to the initial gas mass. K13 gave the equations for each model. We fit the models using an MCMC, as described by K13.

Figure 6 shows the MDFs for each dSph along with the best-fit chemical evolution models. The parameters for the models are given in Table 5. The dSphs are ordered left to right in Figure 6 from high to low stellar mass. Two trends are apparent. First, the MZR is reflected in the way that the peaks of the MDFs shift more metal-poor with decreasing M_* . Second, only the most massive dSph, And VII, fits the Pre-Enriched Model. We could measure only upper limits to $[\text{Fe}/\text{H}]_0$ in And I, III, V, and X. In the limit $[\text{Fe}/\text{H}]_0 \rightarrow -\infty$, the Pre-Enriched Model devolves into the Leaky Box Model. For that reason, the Pre-Enriched Model (green) is overlapped by the Leaky Box Model (blue).

However, there is no apparent trend for which model fits best. We assessed the best model with the corrected Akaike information criterion (AICc Akaike 1974; Sugiyama 1978). The AICc evaluates the goodness of fit of a model with a penalty on the number of free parameters. More complex models must overcome this penalty to be the favored model. The most meaningful way to interpret the AICc is the difference in AICc between two models: ΔAICc . Table 5 gives ΔAICc compared against the Leaky Box Model. Positive values of ΔAICc for the Pre-Enriched and Accretion Models indicate that they are preferred over the Leaky Box Model. Jeffreys’s

(1998) scale suggests a way to interpret ΔAICc , which is approximately twice the natural logarithm of the ratio of the likelihoods of the two models. Values greater than 2.3, 4.6, and 9.2 constitute “substantial,” “strong,” and “decisive” evidence, respectively. Between the Pre-Enriched and Accretion Models, the preferred model has the larger ΔAICc . And VII is the only model where the Pre-Enriched Model fits best. The Accretion Model fits And I and And V the best. The Leaky Box Model is an adequate fit to And III and And X with no need for any free parameters beyond p_{eff} .

Ho et al. (2015) found that the Leaky Box Model is a good fit to the MDF of And VII, in tension with our conclusion. Their MDF included 107 stars, which is an even larger sample than ours. The major differences between the two studies are the exposure times and the measurement technique employed. Our exposure times were at least five times longer than those of Ho et al. (2015). We also use spectral synthesis of Fe I lines rather than the equivalent widths of the Ca II infrared triplet. We suggest that both factors result in smaller random and systematic errors in our measurements. We conclude the MDF of And VII is inconsistent with the Leaky Box Model.

Extremely metal-poor (EMP, $[\text{Fe}/\text{H}] < -3$) stars are interesting because they presumably formed very early in the history of the Universe. Our sample contains six EMP stars: three each in And V and And X. The absence of EMP stars in And VII, And I, and And III is consistent with their best-fit chemical evolution models, which predict less than one EMP star in each dSph. The best-fit models for And V and And X predict 1.6 and 1.9 EMP stars, respectively. These predictions are consistent within Poisson uncertainty with the three observed EMP stars in each dSph.

4.3. Comparison of M31 dSphs to MW dSphs

It is illustrative to compare the MDFs of M31 dSphs with those of MW dSphs of similar metallicity or stellar mass. Figure 7 shows the M31 dSph MDFs with the MDF of the MW dSph with the closest $\langle[\text{Fe}/\text{H}]\rangle$ in the

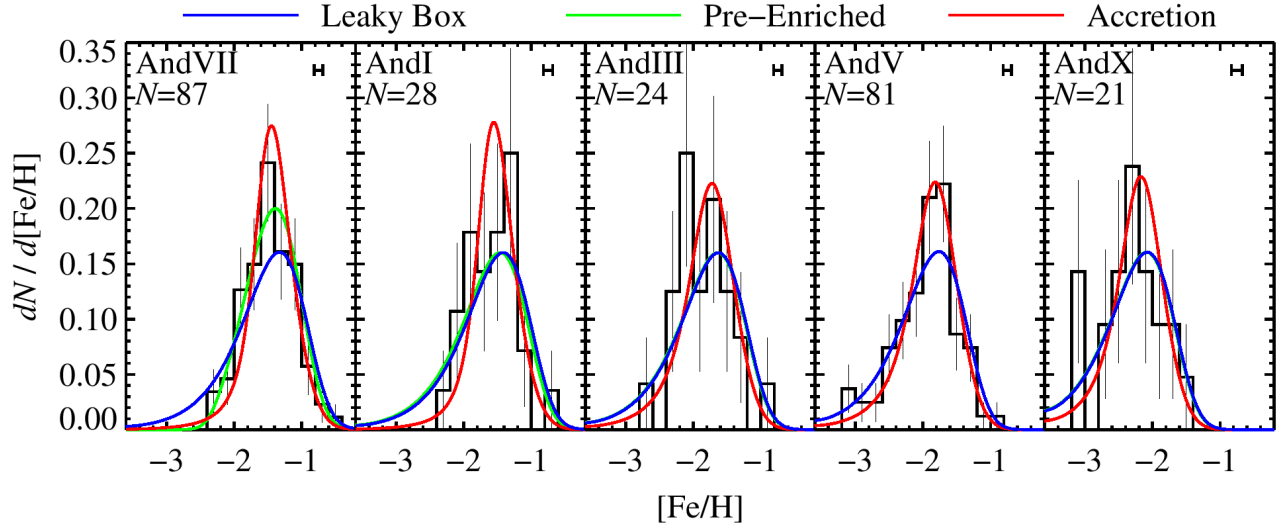


Figure 6. The MDFs of M31 dSphs in bins of 0.2 dex. Error bars are Poissonian. Only stars with errors less than 0.4 dex contribute to the MDFs. The error bars in the upper right of each panel show median uncertainties in $[\text{Fe}/\text{H}]$. Best-fit chemical evolution models are shown as colored curves. The curves are convolved with a function to approximate the widening induced by observational uncertainty, as described in the caption to Figure 4. The Pre-Enriched Model is a generalization of the Leaky Box Model, where the initial metallicity is allowed to be non-zero. The Accretion Model is a different generalization of the Leaky Box Model that allows gas infall. The green curves are not visible in the right three panels because the blue curves completely overlap them. Section 4 describes the chemical evolution models, and Table 5 gives the best-fit parameters of each model.

Table 5. Chemical Evolution Models

dSph	Leaky Box	Pre-Enriched		Accretion			Best Model	
	$p_{\text{eff}}^a (Z_{\odot})$	$p_{\text{eff}}^a (Z_{\odot})$	$[\text{Fe}/\text{H}]_0^b$	ΔAICc^c	$p_{\text{eff}}^a (Z_{\odot})$	M^d		ΔAICc^c
And VII	0.049 ± 0.006	$0.038_{-0.005}^{+0.006}$	$-2.40_{-0.17}^{+0.13}$	15.94	0.044 ± 0.004	$5.9_{-2.5}^{+4.2}$	10.28	Pre-Enriched
And I	$0.040_{-0.008}^{+0.009}$	$0.036_{-0.009}^{+0.010}$	< -2.18	-2.24	$0.035_{-0.005}^{+0.006}$	$6.4_{-3.2}^{+4.4}$	3.72	Accretion
And III	$0.025_{-0.005}^{+0.007}$	$0.024_{-0.005}^{+0.007}$	< -2.83	-2.31	$0.021_{-0.004}^{+0.005}$	$2.6_{-1.1}^{+2.0}$	-1.83	Leaky Box
And V	$0.018_{-0.002}^{+0.003}$	$0.018_{-0.002}^{+0.003}$	< -16.65	-2.10	0.017 ± 0.002	$2.5_{-0.7}^{+1.1}$	4.47	Accretion
And X	$0.009_{-0.002}^{+0.003}$	$0.009_{-0.002}^{+0.003}$	< -3.51	-2.38	0.008 ± 0.002	$2.7_{-1.2}^{+2.7}$	-2.21	Leaky Box

NOTE—Error bars represent 68% confidence intervals. Upper limits are at 95% (2σ) confidence.

^aEffective yield.

^bInitial metallicity.

^cDifference in the corrected Akaike information criterion between the specified model and the Leaky Box model. Positive numbers indicate that the specified model is preferred over the Leaky Box model.

^dAccretion parameter, which is the ratio of final stellar mass to initial gas mass.

sample of K13.⁵ We expect the MW dSph MDFs to be slightly narrower than the M31 dSph MDFs because the

uncertainties are smaller for the MW dSphs. Indeed, the MDF of Leo I is slightly narrower than that of And VII but otherwise similar. The other dSph pairs show some differences. And I lacks very metal-poor stars compared to Leo II. And III has a symmetric MDF compared to Sculptor, which shows a sharp metal-rich cut-off. K13 explained the cut-off as an effect of ram pressure stripping. The MDF of And V is actually slightly narrower

⁵ Strictly speaking, Leo I ($\langle[\text{Fe}/\text{H}]\rangle = -1.45$) has the closest $\langle[\text{Fe}/\text{H}]\rangle$ to both And VII and And I, but we compare And I with the next closest match, Leo II ($\langle[\text{Fe}/\text{H}]\rangle = -1.63$), to show a larger diversity of MW dSph MDFs.

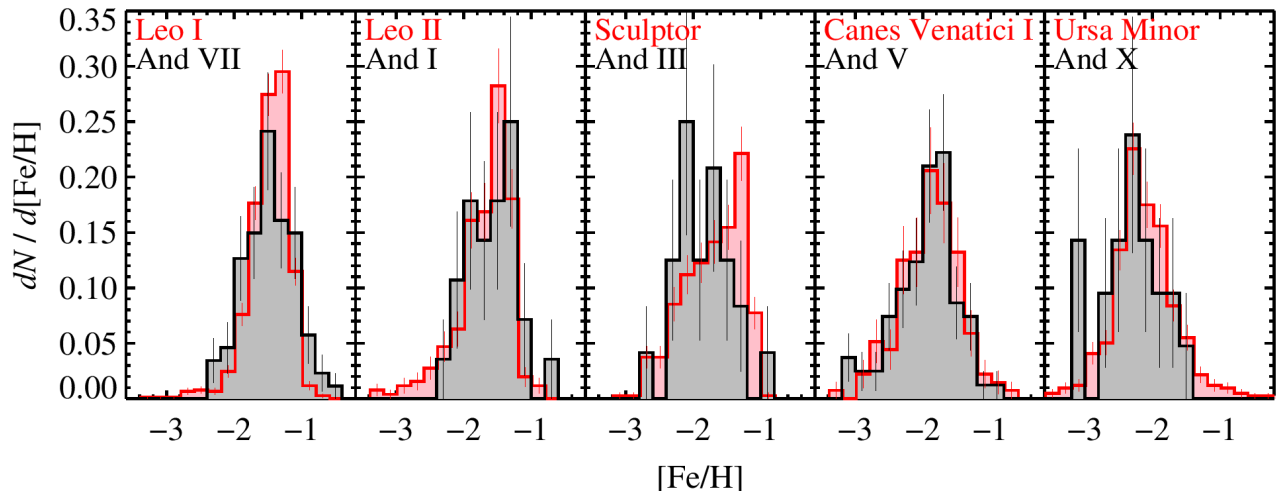


Figure 7. MDFs of M31 dSphs shown with corresponding MDFs of MW dSphs (Kirby et al. 2010, 2011b) of similar average metallicity. The MDFs are measured with identical techniques. Error bars are Poissonian. Only stars with errors less than 0.4 dex contribute to the MDFs. Section 4 discusses the comparison between the pairs of MDFs.

than that of Canes Venatici I, which explains why And V favors the Accretion Model. Gas accretion sets up an equilibrium metallicity that causes stars to form in a narrow range of $[\text{Fe}/\text{H}]$. And X lacks metal-rich stars compared to Ursa Minor. However, Ursa Minor is unusual for having a metal-rich tail.

The similarity in MDF shapes extends to derived chemical evolution model parameters. For example, K13 found that the MDF of Leo I was best fit by the Accretion Model with $p_{\text{eff}} = 0.043 \pm 0.001$ and $M = 7.9^{+1.2}_{-1.0}$. Although And VII formally prefers the Pre-Enriched Model, its best-fit Accretion Model has p_{eff} and M perfectly in line with those of Leo I. The agreement between model parameters persists for most of the other dSph pairs, even if the preferred model is not always the same. The exception is And X. Its MW counterpart, Ursa Minor, has a best-fit accretion parameter of $M = 11.0^{+5.6}_{-4.5}$, which is inconsistent with our determination of M for And X. We suggest that none of these models is a particularly good fit to Ursa Minor because of its metal-rich tail.

There is significant diversity in MDF shapes in MW dSphs even at similar $\langle[\text{Fe}/\text{H}]\rangle$. As an example, Figure 7 would not give the impression that the MW and M31 dSphs agreed very well if we chose the MW dSph with the closest M_* rather than the closest $\langle[\text{Fe}/\text{H}]\rangle$. Given the diversity of MDF shapes and the sample sizes in the M31 dSphs, we do not have any reason to conclude that the M31 satellites experienced a different metallicity enrichment history as a function of stellar mass from that of the MW satellites.

5. ALPHA ELEMENT ENHANCEMENT

In this section, we present $[\alpha/\text{Fe}]$ ratios for And I, III, V, VII, and X. These are a subset of the dSphs studied by V14a, but the spectra used here have much higher SNR. As a result, we are able to measure not only a

single “alpha” abundance but also individual element ratios, like $[\text{Si}/\text{Fe}]$. We discuss qualitative trends in the $[\alpha/\text{Fe}]$ vs. $[\text{Fe}/\text{H}]$ diagram, and we provide some quantitative metrics of chemical evolution. We also compare the distributions of abundance ratios in the M31 satellites to those of the MW satellites.

Figure 8 shows the trends of $[\alpha/\text{Fe}]$ with $[\text{Fe}/\text{H}]$. The dSphs are listed from top to bottom in order of decreasing stellar mass. The MZR is reflected by the leftward (decreasing $[\text{Fe}/\text{H}]$) shift for decreasing M_* . Although the average metallicities of the stars vary across the dSphs, all of the galaxies exhibit a decrease of $[\alpha/\text{Fe}]$ with $[\text{Fe}/\text{H}]$.

We calculated the slopes of $[\alpha/\text{Fe}]$ vs. $[\text{Fe}/\text{H}]$ by using maximum likelihood coupled with a Monte Carlo Markov chain (MCMC). The likelihood function parameterizes the line by an angle θ and a perpendicular offset b_{\perp} .

$$[\alpha/\text{Fe}] = [\text{Fe}/\text{H}] \tan \theta + \frac{b_{\perp}}{\cos \theta} \quad (4)$$

We adopted flat priors on θ and b_{\perp} .⁶ This parameterization avoids the bias against steep slopes when the line is parameterized by $y = mx + b$ and a flat prior is adopted for m (see Hogg et al. 2010). The conversions between the two parameterizations are $m = \tan \theta$ and $b_{\perp} = b \cos \theta$. We found the best-fit slope with an MCMC of 10^6 links following a burn-in period of 10^5 links. The MCMC is based on the Metropolis algorithm. The slopes $m = d[\alpha/\text{Fe}]/d[\text{Fe}/\text{H}]$ are given in Table 6 and also shown in Figure 9. The values given are the 50th percentiles of the MCMC chains with 68% C.L. error bars at the 16th and 84th percentiles.

⁶ This procedure is identical to that of J. Wojno et al. (in preparation).

Table 6. Abundance Trends in dSphs

DSph	$\log(M_*/M_\odot)^a$	$\log(M_{1/2}/M_\odot)^b$	$\langle[\text{Fe}/\text{H}]\rangle$	$d[\alpha/\text{Fe}]/d[\text{Fe}/\text{H}]$
M31 dSphs				
And VII	7.21 ± 0.12	8.08 ± 0.08	-1.37 ± 0.01	$-0.42^{+0.09}_{-0.10}$
And I	6.86 ± 0.40	$7.71^{+0.16}_{-0.14}$	-1.51 ± 0.02	$-0.96^{+0.24}_{-0.24}$
And III	6.27 ± 0.12	$7.65^{+0.15}_{-0.13}$	-1.75 ± 0.03	$-0.79^{+0.14}_{-0.14}$
And V	5.81 ± 0.12	7.59 ± 0.08	-1.84 ± 0.01	$-0.53^{+0.09}_{-0.09}$
And X	5.08 ± 0.03	$6.82^{+0.22}_{-0.20}$	-2.27 ± 0.03	$-1.00^{+0.28}_{-0.29}$
MW dSphs				
Fornax	7.39 ± 0.14	7.87 ± 0.02	-1.04 ± 0.01	$+0.02^{+0.04}_{-0.04}$
Leo I	6.69 ± 0.13	7.34 ± 0.05	-1.45 ± 0.01	$-0.21^{+0.03}_{-0.03}$
Sculptor	6.59 ± 0.21	7.35 ± 0.03	-1.68 ± 0.01	$-0.43^{+0.02}_{-0.02}$
Leo II	6.07 ± 0.13	$6.86^{+0.07}_{-0.06}$	-1.63 ± 0.01	$-0.26^{+0.04}_{-0.04}$
Sextans	5.84 ± 0.20	$7.54^{+0.07}_{-0.06}$	-1.94 ± 0.01	$-0.56^{+0.07}_{-0.08}$
Ursa Minor	5.73 ± 0.20	7.75 ± 0.06	-2.13 ± 0.01	$-0.57^{+0.03}_{-0.03}$
Draco	5.51 ± 0.10	7.32 ± 0.06	-1.98 ± 0.01	$-0.44^{+0.04}_{-0.05}$
Canes Venatici I	5.48 ± 0.09	$7.44^{+0.13}_{-0.10}$	-1.91 ± 0.01	$-0.55^{+0.07}_{-0.07}$

^aStellar mass calculated from the product of luminosity and stellar mass-to-light ratio (Woo et al. 2008). The luminosities were measured by Martin et al. (2008, Canes Venatici I) and Tollerud et al. (2012, M31 dSphs) or otherwise compiled by McConnachie (2012).

^bMass within the half-light radius, taken from Table 3.

NOTE—Dynamical masses for MW dSphs were taken from Wolf et al. (2010). Abundance information for MW dSphs was drawn from K13.

A slope of -1 would indicate constant $[\alpha/\text{H}]$, i.e., enrichment solely by Type Ia supernovae with no contributions from core collapse supernovae. The shallowness of the slope (Table 6) for And VII, the most massive dSph in our sample, indicates that it maintained a higher average SFR during its star-forming lifetime than the other dSphs. The higher SFR allowed it to create a higher ratio of core collapse to Type Ia supernovae. The steeper slopes of the less massive dSphs reflect inefficient SFHs, wherein Type Ia supernovae dominated the chemical evolution.

It could be reasonably expected that the abundance patterns of dwarf galaxies are more closely related to their dynamical masses than their stellar masses. After all, it is the depth of the gravitational potential well that dictates the galaxy’s ability to retain metals (Dekel & Silk 1986). Table 6 shows that the average metallicities and $[\alpha/\text{Fe}]$ slopes of M31 dSphs are reasonably well correlated with dynamical mass. However,

there is essentially no correlation between dynamical mass and stellar mass or abundance properties of MW dSphs, as discussed previously in the literature (e.g., Strigari et al. 2008; Kirby et al. 2011b). One possibility is that the dark matter in dSphs is much more extended than the stellar distribution. It is therefore difficult to measure the full depth of the gravitational potential because there are no luminous tracers of the mass at large radii. Unfortunately, our sample size of five M31 dSphs is not sufficient to make definitive statements about whether the M31 system has a stronger correlation between abundances and dynamical mass than the MW system.

Figure 8 also shows MW dSphs with average metallicities comparable to those of the M31 dSphs. The MW dSphs are the same as those shown in Figure 7. Like the MDFs, there is enough diversity in the $[\alpha/\text{Fe}]$ diagrams among dSphs of similar $\langle[\text{Fe}/\text{H}]\rangle$ that our ability to draw quantitative conclusions is limited. However, there are

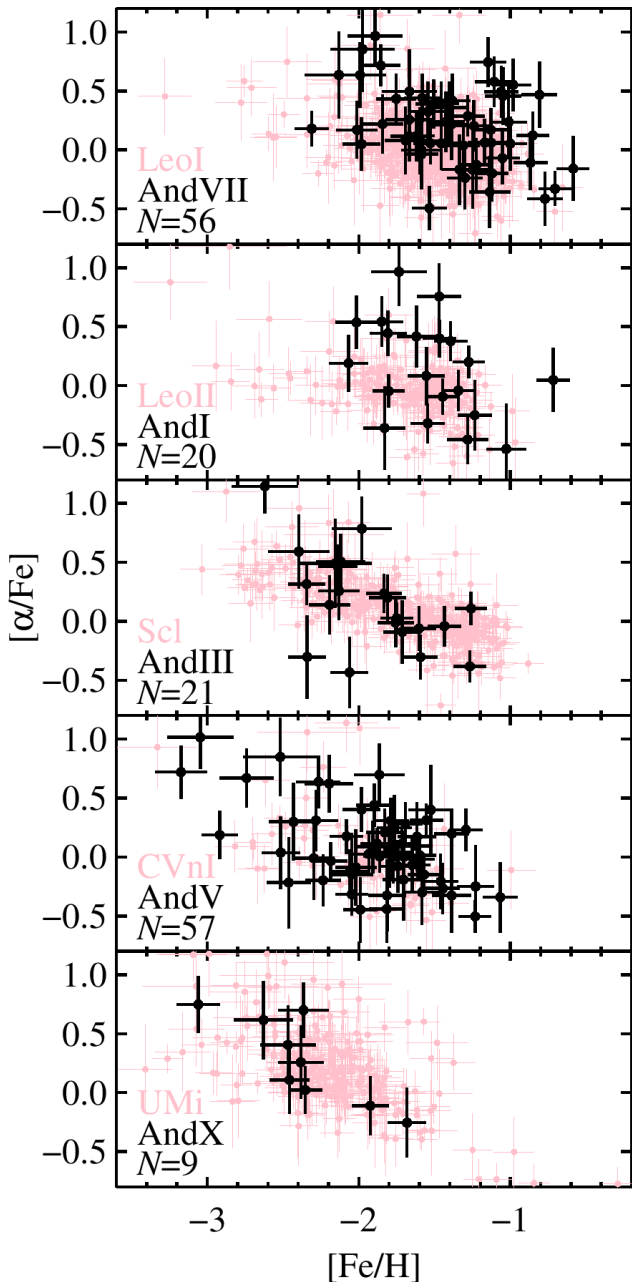


Figure 8. Trends of $[\alpha/\text{Fe}]$ with $[\text{Fe}/\text{H}]$. The M31 dSphs are shown in black. In the same panel, the MW dSph with the closest $\langle[\text{Fe}/\text{H}]\rangle$ is shown in pink (Kirby et al. 2010, 2011a), as in Figure 7. The more massive, metal-rich dSphs have shallower slopes (Table 6) because they maintained higher SFRs. Section 2.4 describe the abundance measurements, and Section 5 discusses their significance.

some qualitative trends as a function of M_* that persist in both the MW and M31 samples. We describe some of these trends below.

Table 6 shows the $d[\alpha/\text{Fe}]/d[\text{Fe}/\text{H}]$ slopes of the MW dSphs alongside those of the M31 dSphs. The slopes are generally steeper for dSphs of lower M_* . This trend

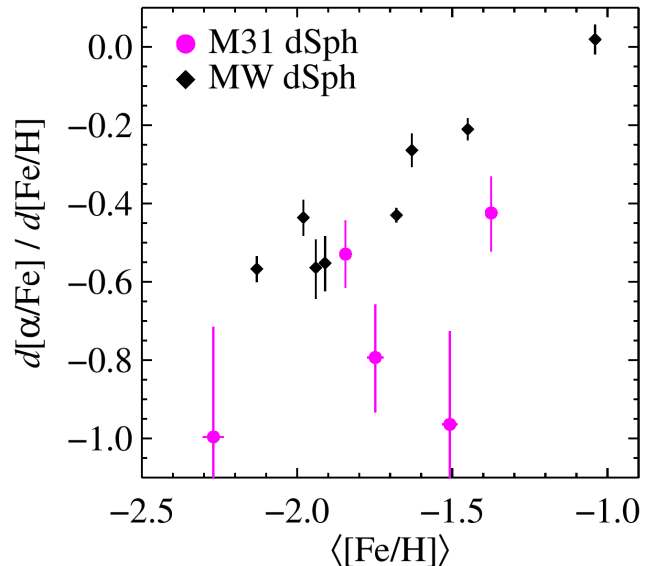


Figure 9. The slopes of $[\alpha/\text{Fe}]$ vs. $[\text{Fe}/\text{H}]$ in M31 dSphs (magenta circles) and MW dSphs (black diamonds).

is consistent with the concept that satellites of both the MW and M31 systems that were able to maintain higher SFRs, as reflected by shallower $[\alpha/\text{Fe}]$ slopes, were also able to reach higher stellar masses (also see Tolstoy et al. 2009; Letarte et al. 2010; Kirby et al. 2011a; Lemasle et al. 2014).

Shallower $[\alpha/\text{Fe}]$ slopes accompany MDFs that are inconsistent with a simple Leaky Box. This correlation can be seen by comparing Table 5 to Table 6. More massive dSphs have narrower MDFs that favor the Pre-Enriched or Accretion Models. The MDFs suggest that more massive dSphs evolved in the presence of an external influence, such as gas accretion. It is possible that these dSphs were able to maintain higher SFRs for a longer period of time because they had access to an external gas reservoir. That could be why they grew to larger stellar mass. The tendency for more efficient star formers (reflected in the $[\alpha/\text{Fe}]$ slope) to have access to external gas (reflected in the MDF shape) is present in both the MW dSphs (Kirby et al. 2011b; K13) and the M31 dSphs.

Skillman et al. (2017) measured the SFHs of And I and And III, among other M31 satellites, with *Hubble Space Telescope* (*HST*) imaging reaching the main sequence turn-off (MSTO). Skillman et al. found more uniformity in the SFHs among the M31 dSphs than the MW dSphs. For example, the MW has three dSphs in the $10^{6-7} M_\odot$ range of stellar mass: Leo I, Sculptor, and Leo II. They have extended, ancient, and intermediate SFHs, respectively (Weisz et al. 2014). In contrast, And I and And III, which also fall in that stellar mass range, both have intermediate SFHs (Skillman et al. 2017).

From shallower *HST* imaging, Weisz et al. (2014) measured the SFHs of And VII, I, III, and V. The SFHs of And I and And III are consistent with those of Skillman et al. (2017). Interestingly, Weisz et al. found that the SFH of And VII was as ancient as that of Sculptor. The $[\alpha/\text{Fe}]$ pattern of And VII is difficult to reconcile with an ancient SFH. All of the MW dSphs with exclusively old populations have $\langle[\text{Fe}/\text{H}]\rangle < -1.5$ as well as steeply declining $[\alpha/\text{Fe}]$. In contrast, And VII has $\langle[\text{Fe}/\text{H}]\rangle = -2.27 \pm 0.03$, as well as the shallowest $d[\alpha/\text{Fe}]/d[\text{Fe}/\text{H}]$ of all the M31 dSphs in our sample. And VII is part of an upcoming, large Cycle 27 *HST* program (GO-15902, PI: D. Weisz). The purpose of the program is to obtain CMDs of M31 dSphs that reach the MSTO, i.e., quality comparable to those obtained by Skillman et al. (2017). It will be interesting to see if And VII continues to appear exclusively ancient in these high-quality measurements.

The preference for M31 dSphs to have extended SFHs or at least intermediate-age populations may extend to its least massive satellites ($M_* < 10^{5.5} M_\odot$). Martin et al. (2017) analyzed *HST*-based CMDs of some of the less massive M31 dSphs, including And X. These CMDs reached the horizontal branch (HB) but not the MSTO. Even the faintest M31 dSphs in their sample ($10^{4.2} L_\odot$) have red HBs, which probably indicate the presence of intermediate-age populations that are not very metal-poor. In contrast, low-mass MW dSphs have more prominent blue HBs than red HBs. From the perspective of chemical evolution, And X appears to have an $[\alpha/\text{Fe}]$ distribution consistent with MW dSphs of similar metallicity (Ursa Minor) or slightly larger stellar mass (Canes Venatici I), though we measured $[\alpha/\text{Fe}]$ for only 9 stars in And X. *HST* CMDs show Ursa Minor and Canes Venatici I to have slightly older populations than And I and And III (Weisz et al. 2014; Skillman et al. 2017). It is not yet possible to confirm whether And X’s HB morphology results from a more extended SFH than its MW counterparts because it does not yet have imaging deep enough to reach the MSTO. However, And X will be observed as part of the aforementioned *HST* large program.

Our deep DEIMOS spectroscopy enables us for the first time to measure individual element ratios in the M31 system. Figure 10 shows $[\text{Mg}/\text{Fe}]$, $[\text{Si}/\text{Fe}]$, $[\text{Ca}/\text{Fe}]$, and $[\text{Ti}/\text{Fe}]$ ratios for the five M31 dSphs in our sample. Each panel shows all five dSphs to emphasize the difference in $[\alpha/\text{Fe}]$ distributions across a range of dSph mass. The figure excludes measurements with uncertainties greater than 0.4 dex in either axis. As a result, there is a bias against stars with low $[\text{Mg}/\text{Fe}]$ and $[\text{Si}/\text{Fe}]$, especially at low $[\text{Fe}/\text{H}]$. The absorption lines of Ca and Ti are generally of lower excitation potential and thus stronger in red giants (see Table 3 of Kirby et al. 2010). Therefore, the bias against low abundances is not as strong for $[\text{Ca}/\text{Fe}]$ and $[\text{Ti}/\text{Fe}]$. Appendix B further discusses the bias against stars with low $[\alpha/\text{Fe}]$

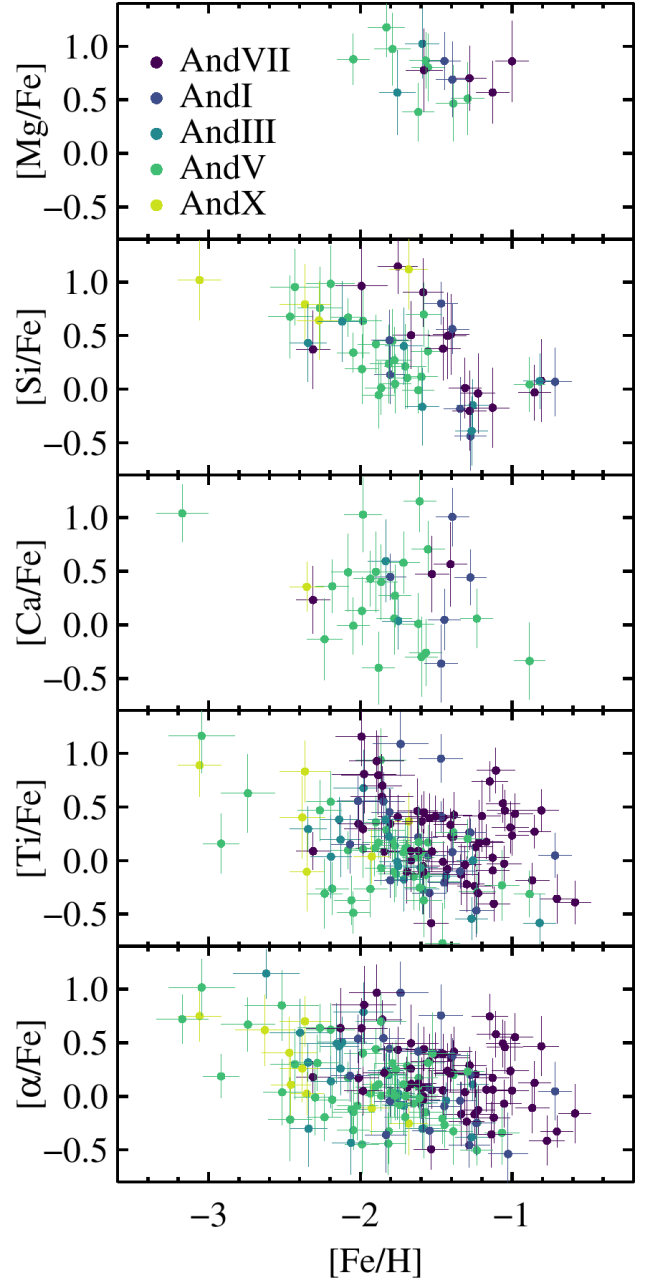


Figure 10. Distribution of individual α element ratios (top four panels) and $[\alpha/\text{Fe}]$ (bottom panel; measured from the union of Mg, Si, Ca, and Ti absorption lines) as a function of $[\text{Fe}/\text{H}]$. Each M31 dSph is shown with a different color. Only measurements with uncertainties less than 0.4 dex are shown. This error cut imposes a bias against including stars with low values of $[\text{Mg}/\text{Fe}]$ and $[\text{Si}/\text{Fe}]$ (see Section 5). The legend lists the dSphs from largest to smallest stellar mass.

ratios. The bottom panel of Figure 10, $[\alpha/\text{Fe}]$, is not an average of the top four panels. Instead, it is a measurement based on the union of Mg, Si, Ca, and Ti absorption lines, as described at the end of Section 2.4.

(This use of $[\alpha/\text{Fe}]$ is consistent with the rest of this paper.) Measuring $[\alpha/\text{Fe}]$ is possible at lower metallicity than individual element ratios because inclusion of a larger number of absorption lines increases the SNR of the measurement.

The dSphs form a tidy $[\alpha/\text{Fe}]$ - $[\text{Fe}/\text{H}]$ sequence in stellar mass. Although each dSph shows a decline in $[\alpha/\text{Fe}]$, the average $[\alpha/\text{Fe}]$ at fixed $[\text{Fe}/\text{H}]$ declines with stellar mass. We have already seen that the $d[\alpha/\text{Fe}]/d[\text{Fe}/\text{H}]$ slope steepens with decreasing M_* . Figure 10 additionally makes clear that $[\alpha/\text{Fe}]$ begins to decline at lower $[\text{Fe}/\text{H}]$ in lower-mass dSphs. The general appearance is that declining $[\alpha/\text{Fe}]$ trends shifts to lower $[\text{Fe}/\text{H}]$ and becomes steeper as M_* decreases.

The most straightforward interpretation of these trends is that low-mass galaxies were susceptible to both heavy gas loss and inefficient star formation. The gas loss suppressed the rate at which $[\text{Fe}/\text{H}]$ increased, as discussed in relation to the Leaky Box Model in Section 4. The low SFRs permitted the rate of Type Ia supernovae to overtake the rate of core collapse supernovae. Larger galaxies retained more gas and metals, allowing them to reach higher $[\text{Fe}/\text{H}]$. They also had higher SFRs, which allowed them to delay the diminution of $[\alpha/\text{Fe}]$ to higher metallicity.

The trends with stellar mass are apparent both in the bulk $[\alpha/\text{Fe}]$ ratio as well as individual ratios, especially $[\text{Si}/\text{Fe}]$ and $[\text{Ti}/\text{Fe}]$. Of these two elements, Si better discriminates between Type Ia and core collapse supernovae. Si is made almost entirely in core collapse supernovae (i.e., Woosley & Weaver 1995; Kirby et al. 2019), but Ti is made in both types of supernovae. Furthermore, most theoretical predictions of Ti yields from core collapse supernovae miss the abundances of metal-poor halo stars by a factor of several (Nomoto et al. 2006; Kirby et al. 2011a; Kobayashi et al. 2011). Nonetheless, Ti has long been observed to mimic the pattern of “true” α elements (i.e., Venn et al. 2004). Our observations support this observation. For example, the $[\text{Ti}/\text{Fe}]$ measurements follow the same trends as the $[\text{Si}/\text{Fe}]$ measurements.

6. M31’S SATELLITES IN THE CONTEXT OF HALO ASSEMBLY

In this section, we compare the abundance trends of M31’s largest intact dSph⁷, And VII, with the GSS and M31’s smooth halo. One purpose of this comparison is to consider the extent to which galaxies similar to M31’s surviving dSphs could have contributed to its stellar halo. A similar comparison in the MW system shows that the inner halo is composed primarily of galax-

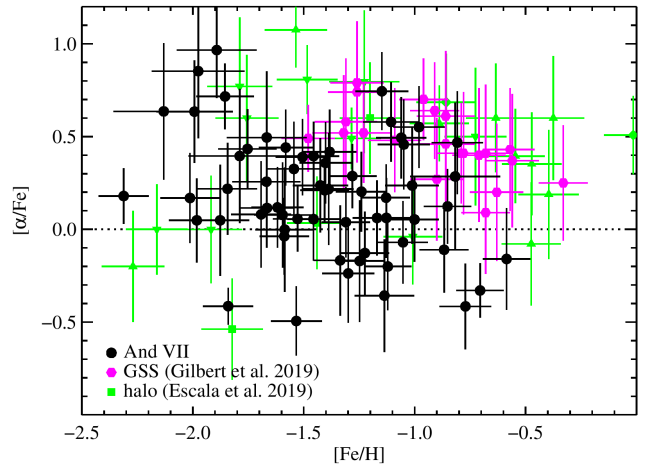


Figure 11. Comparison of the abundance trends of And VII with the GSS (Gilbert et al. 2019) and M31’s smooth halo (Escala et al. 2019a). Only stars with uncertainties less than 0.4 dex in both axes are shown. The figure excludes stars with TiO absorption and halo stars with a probability greater than 50% of belonging to kinematic substructure. The shapes of the halo points identify the fields to which they belong: H (squares), S (diamonds), D (upward-pointing triangles), and f130.2 (downward-pointing triangles). As found by Gilbert et al. (2019) and Escala et al. (2019a), the chemical abundance patterns of M31 dSphs are inconsistent with those of the GSS and the metal-rich, inner halo. Section 6 interprets the different abundance patterns in these systems in the context of the hierarchical formation of stellar halos.

ies that were larger than the largest surviving dSphs (Shetrone et al. 2001, 2003; Venn et al. 2004).

We use the measurements of $[\text{Fe}/\text{H}]$ and $[\alpha/\text{Fe}]$ from previous papers in this series: Gilbert et al. (2019) for the GSS and Escala et al. (2019a) for the smooth halo. We consider only measurements with uncertainties less than 0.4 dex in both $[\text{Fe}/\text{H}]$ and $[\alpha/\text{Fe}]$. Escala et al. (2019a) analyzed four separate fields, called H, S, D, and f130.2. The fields roughly correspond to the halo (at 12 kpc projected from the center of M31), GSS, outer disk, and a different part of the halo (at 23 kpc). In detail, each field contains some stars that belong to the smooth halo and some stars that belong to kinematic substructure. We omit stars more likely to belong to substructure than the halo, i.e., stars with substructure probability greater than 50%. We also omit stars that have TiO absorption that could distort the abundance measurements. Gilbert et al. (2019) used the same DEIMOS configuration (1200G grating) and abundance measurement technique as we used for the dSphs. Escala et al. (2019a) used a lower spectral resolution and wider wavelength range (600ZD grating) and an abundance code adapted to take advantage of the larger spectral range. Escala et al. (2019b) demonstrated the consistency of the two techniques.

⁷ We are considering that M32 is a compact elliptical and NGC 147, NGC 185, and NGC 205 are dwarf ellipticals, not dSphs, but the distinction is admittedly arbitrary (see McConnachie 2012).

Figure 11 shows the trends of $[\alpha/\text{Fe}]$ with $[\text{Fe}/\text{H}]$ for And VII, the GSS, and the smooth halo. It is immediately clear that each component has a distinct chemical evolution. And VII is more metal-poor on average than the GSS and the halo. It also has lower $[\alpha/\text{Fe}]$ ratios at $[\text{Fe}/\text{H}] \gtrsim -1.5$. The chemical distinction from the GSS and halo is even more severe for M31 satellites smaller than And VII, as shown in Section 5. We did not show them in Figure 11 for clarity.

This comparison leads us to echo one of the conclusions of Escala et al. (2019a). Namely, M31’s inner halo with $[\text{Fe}/\text{H}] \gtrsim -1.5$ is not predominantly composed of dwarf galaxies similar to its surviving dSphs. The average halo star is more metal-rich and more α -enhanced. The MZR (Figure 5) implies that the typical halo star originated in a galaxy more massive than even And VII. The mean metallicity of the halo stars in Figure 11 is $\langle [\text{Fe}/\text{H}] \rangle = -1.12 \pm 0.03$. Although these halo stars have a complicated selection function and could originate from more than one accretion event, it is clear that the typical halo star is more metal-rich and α -enhanced than the typical star in And VII. If we assume that the halo stars arose from a single progenitor, the stellar mass corresponding to its mean metallicity (K13) would be $(8 \pm 4) \times 10^7 M_\odot$, five times larger than And VII. The halo progenitors also experienced more efficient star formation, which allowed them to maintain high $[\alpha/\text{Fe}]$ to a higher metallicity than And VII.

We also restate one of the conclusions of Gilbert et al. (2019): The progenitor to the GSS was more metal-rich, and therefore more massive, than M31’s surviving dSphs. Gilbert et al. estimated from the MZR that its original stellar mass was between $5 \times 10^8 M_\odot$ and $2 \times 10^9 M_\odot$ or possibly higher, given the sample biases. In contrast, the stellar mass of And VII is $1.6 \times 10^7 M_\odot$, between those of the MW satellites Fornax and Leo I. The decline in $[\alpha/\text{Fe}]$ also began at $[\text{Fe}/\text{H}]$ about 0.8 dex higher in the GSS than in And VII. Therefore, we conclude that And VII had a more inefficient SFH, with more gas loss and a chemical evolution dominated by Type Ia supernovae, compared to the GSS.

Figure 11 is a synopsis of the past, present, and future of the hierarchical structure formation predicted by Λ CDM (Robertson et al. 2005; Bullock & Johnston 2005; Font et al. 2006; Johnston et al. 2008). In the past, the nascent M31 accreted a small number of large dwarf galaxies that experienced high SFRs until the time of accretion. The stars from these galaxies have now phase-mixed into the smooth halo. In the present, M31 is accreting other dwarf galaxies that likely collapsed later in the Universe. The GSS and Sagittarius are two examples of present-day accretion in M31 and the MW, respectively. In the future, the outer halo of M31 will accrete some of its even smaller, intact satellites that have yet to experience severe tidal disruption. And VII and the other dSphs in this study are examples of small,

intact dwarf galaxies that may dissolve into the outer halo in the distant future.

7. SUMMARY

We presented deep Keck/DEIMOS spectroscopy of five dSph satellites of M31 spanning a stellar mass range from $1.2 \times 10^5 M_\odot$ to $1.6 \times 10^7 M_\odot$. These dSphs are a subset of those with previously published shallow spectroscopy (V14a). The exposure times (ranging from 4.6 to 11.7 hours) enabled us to achieve SNR up to an unprecedented 73 \AA^{-1} for individual member stars. We measured $[\text{Fe}/\text{H}]$ and $[\alpha/\text{Fe}]$ for those stars, with errors as low as 0.10 dex and 0.12 dex, respectively. We even measured the individual abundance ratios $[\text{Mg}/\text{Fe}]$, $[\text{Si}/\text{Fe}]$, $[\text{Ca}/\text{Fe}]$, and $[\text{Ti}/\text{Fe}]$ where possible. We identified 256 member stars across all five dSphs on the basis of radial velocity, CMD position, and the strength of the Na I doublet. We obtained measurements of $[\text{Fe}/\text{H}]$ and $[\alpha/\text{Fe}]$ for 241 and 163 stars, respectively.

We measured the velocity dispersions and mass-to-light ratios of the dSphs, and we found them to be consistent with previous measurements (Tollerud et al. 2012). The majority of the mass in all of the dSphs is dark matter. We also found no evidence for galactic rotation. We placed upper limits on the rotation velocity between 6 and 10 km s^{-1} .

The M31 dSphs obey the same MZR as MW dSphs and other Local Group dwarf galaxies. This conclusion supports past work (K13; V14a), but in contrast to that work, it is based on deep spectroscopy of individual stars. The M31 dSphs’ metallicity distributions have a diversity of shapes. There is no strong evidence for a significant difference between the MDF shapes of M31 and MW dSphs with similar average metallicities. Like the MW dSphs, the largest M31 dSphs disfavor a Leaky Box Model of chemical evolution. Instead, they require pre-enrichment or gas accretion during their star-forming lifetimes.

The $[\alpha/\text{Fe}]$ distributions of the M31 dSphs mimic that of MW dSphs. Each dSph has a negative slope of $[\alpha/\text{Fe}]$ vs. $[\text{Fe}/\text{H}]$, and that slope is generally steeper for dSphs of lower mass. This trend possibly suggests that dSphs of larger stellar mass achieved their larger masses because they were more efficient at forming stars and more resilient to gas outflow. The individual abundance ratios, especially $[\text{Si}/\text{Fe}]$, reinforce the conclusions we drew from the bulk $[\alpha/\text{Fe}]$ ratios.

The M31 dSphs are more metal-poor and exhibit declining $[\alpha/\text{Fe}]$ at lower $[\text{Fe}/\text{H}]$ than the progenitors of the GSS (Gilbert et al. 2019) and M31’s smooth halo (Escala et al. 2019a). This pattern satisfies the prediction of Λ CDM simulations that the inner stellar halos of MW- or M31-like galaxies are composed of large dwarf galaxies that were accreted early. In contrast, smaller galaxies are accreted later into outer regions of the halo. These smaller galaxies have lower metallicities and lower $[\alpha/\text{Fe}]$ at a given $[\text{Fe}/\text{H}]$.

Escala et al. (2019a) measured $[\alpha/\text{Fe}]$ ratios of M31's smooth halo as far out as 23 kpc in projected distance from the center of M31. Escala et al. showed tentative evidence that M31's outer halo (70–140 kpc, Vargas et al. 2014b) has lower $[\alpha/\text{Fe}]$ ratios at a given $[\text{Fe}/\text{H}]$, in line with the prediction that smaller, less efficiently star-forming galaxies are accreted into the outer halo. We predict that additional observations of outer M31 halo stars will show more dSph-like abundance patterns than the inner halo or GSS. Although it is challenging to observe stars in M31's outer halo due to their sparseness and the contamination by MW foreground stars, our series of papers has shown that it is possible to quantify the chemical evolution in a variety of fields in M31. Thus, even before the era of giant telescopes, the M31 system makes possible a test of Λ CDM predictions of detailed abundances complementary to the MW.

ACKNOWLEDGMENTS

We are grateful to Luis Vargas for providing a data table of M31 dSph measurements, including effective temperature. We thank Brent Belland for helpful discussion on the rotation model and Alexander Ji for insightful conversation.

This material is based upon work supported by the National Science Foundation under Grant Nos. AST-1614081 and AST-1614569. ENK gratefully acknowledges support from a Cottrell Scholar award admin-

istered by the Research Corporation for Science Advancement as well as funding from generous donors to the California Institute of Technology. IE acknowledges support from a National Science Foundation (NSF) Graduate Research Fellowship under Grant No. DGE-1745301. PG, SRM, and RLB acknowledge prior funding from collaborative NSF grants AST-0307842, AST-0307851, AST-0607726, AST-0807945, AST-1009882, AST-1009973, and AST-1010039. Support for this work was provided by NASA through Hubble Fellowship grant #51386.01 awarded to RLB by the Space Telescope Science Institute, which is operated by the Association of Universities for Research in Astronomy, Inc., for NASA, under contract NAS 5-26555.

We are grateful to the many people who have worked to make the Keck Telescope and its instruments a reality and to operate and maintain the Keck Observatory. The authors wish to extend special thanks to those of Hawaiian ancestry on whose sacred mountain we are privileged to be guests. Without their generous hospitality, none of the observations presented herein would have been possible. We express our deep gratitude to the staff at academic and telescope facilities whose labor maintains spaces for scientific inquiry.

Facility: Keck:II (DEIMOS)

Software: spec2d (Cooper et al. 2012; Newman et al. 2013), MOOG (Snedden 1973; Sneden et al. 2012), ATLAS9 (Kurucz 1993), MPFIT (Markwardt 2012)

REFERENCES

- Akaike, H. 1974, IEEE Transactions on Automatic Control, 19, 716
- Amorisco, N. C., & Evans, N. W. 2012, ApJL, 756, L2
- Amorisco, N. C., Evans, N. W., & van de Ven, G. 2014, Nature, 507, 335
- Anders, E., & Grevesse, N. 1989, GeoCoA, 53, 197
- Armandroff, T. E., Davies, J. E., & Jacoby, G. H. 1998, AJ, 116, 2287
- Battaglia, G., Helmi, A., Tolstoy, E., et al. 2008a, ApJL, 681, L13
- Battaglia, G., Irwin, M., Tolstoy, E., et al. 2008b, MNRAS, 383, 183
- Battaglia, G., & Starkenburg, E. 2012, A&A, 539, A123
- Beaton, R. L. 2014, PhD thesis, University of Virginia
- Bell, E. F., & de Jong, R. S. 2001, ApJ, 550, 212
- Belokurov, V., Erkal, D., Evans, N. W., Koposov, S. E., & Deason, A. J. 2018, MNRAS, 478, 611
- Brauer, K., Ji, A. P., Frebel, A., et al. 2019, ApJ, 871, 247
- Bullock, J. S., & Johnston, K. V. 2005, ApJ, 635, 931
- Busha, M. T., Wechsler, R. H., Behroozi, P. S., et al. 2011, ApJ, 743, 117
- Collins, M. L. M., Chapman, S. C., Rich, R. M., et al. 2013, ApJ, 768, 172
- Cooper, M. C., Newman, J. A., Davis, M., Finkbeiner, D. P., & Gerke, B. F. 2012, spec2d: DEEP2 DEIMOS Spectral Pipeline, astrophysics Source Code Library, ascl:1203.003
- de Vaucouleurs, G., de Vaucouleurs, A., Corwin, Herold G., J., et al. 1991, Third Reference Catalogue of Bright Galaxies
- Deason, A. J., Belokurov, V., & Weisz, D. R. 2015, MNRAS, 448, L77
- Deason, A. J., Mao, Y.-Y., & Wechsler, R. H. 2016, ApJ, 821, 5
- Dekel, A., & Silk, J. 1986, ApJ, 303, 39
- Dolphin, A. E. 2002, MNRAS, 332, 91
- Escala, I., Gilbert, K. M., Kirby, E. N., et al. 2019a, ApJ, submitted
- Escala, I., Kirby, E. N., Gilbert, K. M., Cunningham, E. C., & Wojno, J. 2019b, ApJ, 878, 42
- Escala, I., Wetzell, A., Kirby, E. N., et al. 2018, MNRAS, 474, 2194

- Faber, S. M., Phillips, A. C., Kibrick, R. I., et al. 2003, in Society of Photo-Optical Instrumentation Engineers (SPIE) Conference Series, Vol. 4841, Instrument Design and Performance for Optical/Infrared Ground-based Telescopes, ed. M. Iye & A. F. M. Moorwood, 1657–1669
- Font, A. S., Johnston, K. V., Bullock, J. S., & Robertson, B. E. 2006, *ApJ*, 638, 585
- Fouquet, S., Lokas, E. L., del Pino, A., & Ebrova, I. 2017, *MNRAS*, 464, 2717
- Geha, M., Wechsler, R. H., Mao, Y.-Y., et al. 2017, *ApJ*, 847, 4
- Geisler, D., Smith, V. V., Wallerstein, G., Gonzalez, G., & Charbonnel, C. 2005, *AJ*, 129, 1428
- Gilbert, K. M., Kirby, E. N., Escala, I., et al. 2019, arXiv e-prints, arXiv:1908.04429
- Gilbert, K. M., Guhathakurta, P., Kollipara, P., et al. 2009, *ApJ*, 705, 1275
- Gilbert, K. M., Guhathakurta, P., Beaton, R. L., et al. 2012, *The Astrophysical Journal*, 760, 76
- Grebel, E. K., Gallagher, John S., I., & Harbeck, D. 2003, *AJ*, 125, 1926
- Grebel, E. K., & Guhathakurta, P. 1999, *ApJL*, 511, L101
- Guhathakurta, P., Rich, R. M., Reitzel, D. B., et al. 2006, *AJ*, 131, 2497
- Hayes, C. R., Majewski, S. R., Shetrone, M., et al. 2018, *The Astrophysical Journal*, 852, 49
- Helmi, A., Babusiaux, C., Koppelman, H. H., et al. 2018, *Nature*, 563, 85
- Hill, V., Skuladottir, A., Tolstoy, E., et al. 2019, *A&A*, 626, A15
- Ho, N., Geha, M., Tollerud, E. J., et al. 2015, *ApJ*, 798, 77
- Ho, N., Geha, M., Munoz, R. R., et al. 2012, *ApJ*, 758, 124
- Hogg, D. W., Bovy, J., & Lang, D. 2010, arXiv:1008.4686
- Ibata, R., Irwin, M., Lewis, G., Ferguson, A. M. N., & Tanvir, N. 2001, *Nature*, 412, 49
- Ibata, R. A., Gilmore, G., & Irwin, M. J. 1994, *Nature*, 370, 194
- Ibata, R. A., Lewis, G. F., McConnachie, A. W., et al. 2014, *ApJ*, 780, 128
- Jeffreys, H. 1998, *The Theory of Probability*, Oxford Classic Texts in the Physical Sciences (OUP Oxford)
- Johnston, K. V., Bullock, J. S., Sharma, S., et al. 2008, *ApJ*, 689, 936
- Kalirai, J. S., Zucker, D. B., Guhathakurta, P., et al. 2009, *ApJ*, 705, 1043
- Kalirai, J. S., Beaton, R. L., Geha, M. C., et al. 2010, *ApJ*, 711, 671
- Karachentsev, I. D., & Karachentseva, V. E. 1999, *A&A*, 341, 355
- Kirby, E. N. 2011, *PASP*, 123, 531
- Kirby, E. N., Cohen, J. G., & Bellazzini, M. 2012, *ApJ*, 751, 46
- Kirby, E. N., Cohen, J. G., Guhathakurta, P., et al. 2013, *ApJ*, 779, 102 (K13)
- Kirby, E. N., Cohen, J. G., Smith, G. H., et al. 2011a, *ApJ*, 727, 79
- Kirby, E. N., Guhathakurta, P., Bolte, M., Sneden, C., & Geha, M. C. 2009, *ApJ*, 705, 328
- Kirby, E. N., Guhathakurta, P., & Sneden, C. 2008, *ApJ*, 682, 1217
- Kirby, E. N., Lanfranchi, G. A., Simon, J. D., Cohen, J. G., & Guhathakurta, P. 2011b, *ApJ*, 727, 78
- Kirby, E. N., Martin, C. L., & Finlator, K. 2011c, *ApJL*, 742, L25
- Kirby, E. N., Rizzi, L., Held, E. V., et al. 2017, *ApJ*, 834, 9
- Kirby, E. N., Simon, J. D., & Cohen, J. G. 2015, *ApJ*, 810, 56
- Kirby, E. N., Guhathakurta, P., Simon, J. D., et al. 2010, *ApJS*, 191, 352
- Kirby, E. N., Xie, J. L., Guo, R., et al. 2019, *ApJ*, 881, 45
- Kobayashi, C., Karakas, A. I., & Umeda, H. 2011, *MNRAS*, 414, 3231
- Kurucz, R. 1993, *ATLAS9 Stellar Atmosphere Programs and 2 km/s grid*. Kurucz CD-ROM No. 13. Cambridge, Mass.: Smithsonian Astrophysical Observatory, 1993., 13
- Lee, D. M., Johnston, K. V., Sen, B., & Jessop, W. 2015, *ApJ*, 802, 48
- Lee, J. C., Gil de Paz, A., Tremonti, C., et al. 2009, *ApJ*, 706, 599
- Lemasle, B., de Boer, T. J. L., Hill, V., et al. 2014, *A&A*, 572, A88
- Lequeux, J., Peimbert, M., Rayo, J. F., Serrano, A., & Torres-Peimbert, S. 1979, *A&A*, 500, 145
- Letarte, B., Hill, V., Tolstoy, E., et al. 2010, *A&A*, 523, A17
- Lokas, E. L., Ebrova, I., Del Pino, A., & Semczuk, M. 2014, *MNRAS*, 445, L6
- Lynden-Bell, D. 1975, *Vistas in Astronomy*, 19, 299
- Majewski, S. R., Ostheimer, J. C., Kunkel, W. E., & Patterson, R. J. 2000, *AJ*, 120, 2550
- Majewski, S. R., Skrutskie, M. F., Weinberg, M. D., & Ostheimer, J. C. 2003, *ApJ*, 599, 1082
- Markwardt, C. 2012, *MPFIT: Robust non-linear least squares curve fitting*, astrophysics Source Code Library, ascl:1208.019
- Martin, N. F., Coleman, M. G., De Jong, J. T. A., et al. 2008, *ApJL*, 672, L13
- Martin, N. F., Ibata, R. A., Lewis, G. F., et al. 2016, *ApJ*, 833, 167
- Martin, N. F., Weisz, D. R., Albers, S. M., et al. 2017, *ApJ*, 850, 16

- Mateo, M. L. 1998, *ARA&A*, 36, 435
- McConnachie, A. W. 2012, *AJ*, 144, 4
- McConnachie, A. W., Irwin, M. J., Ferguson, A. M. N., et al. 2005, *MNRAS*, 356, 979
- Minor, Q. E., Martinez, G., Bullock, J., Kaplinghat, M., & Trainor, R. 2010, *ApJ*, 721, 1142
- Monachesi, A., Bell, E. F., Radburn-Smith, D. J., et al. 2016, *MNRAS*, 457, 1419
- Newman, J. A., Cooper, M. C., Davis, M., et al. 2013, *ApJS*, 208, 5
- Niederste-Ostholt, M., Belokurov, V., Evans, N. W., & Peñarrubia, J. 2010, *ApJ*, 712, 516
- Nomoto, K., Tominaga, N., Umeda, H., Kobayashi, C., & Maeda, K. 2006, *Nuclear Physics A*, 777, 424
- Ostheimer, Jr., J. C. 2003, PhD thesis, UNIVERSITY OF VIRGINIA
- Pace, A. B., Martinez, G. D., Kaplinghat, M., & Muñoz, R. R. 2014, *MNRAS*, 442, 1718
- Pagel, B. E. J. 1997, *Nucleosynthesis and Chemical Evolution of Galaxies*
- Richardson, J. C., Irwin, M. J., McConnachie, A. W., et al. 2011, *ApJ*, 732, 76
- Robertson, B., Bullock, J. S., Font, A. S., Johnston, K. V., & Hernquist, L. 2005, *ApJ*, 632, 872
- Rutledge, G. A., Hesser, J. E., & Stetson, P. B. 1997, *PASP*, 109, 907
- Schmidt, M. 1963, *ApJ*, 137, 758
- Shetrone, M., Venn, K. A., Tolstoy, E., et al. 2003, *AJ*, 125, 684
- Shetrone, M. D., Bolte, M., & Stetson, P. B. 1998, *AJ*, 115, 1888
- Shetrone, M. D., Côté, P., & Sargent, W. L. W. 2001, *ApJ*, 548, 592
- Simon, J. D., & Geha, M. 2007, *ApJ*, 670, 313
- Skillman, E. D., Kennicutt, R. C., & Hodge, P. W. 1989, *ApJ*, 347, 875
- Skillman, E. D., Monelli, M., Weisz, D. R., et al. 2017, *ApJ*, 837, 102
- Snedden, C., Bean, J., Ivans, I., Lucatello, S., & Sobek, J. 2012, MOOG: LTE line analysis and spectrum synthesis, ascl:1202.009
- Snedden, C. A. 1973, PhD thesis, University of Texas Austin.
- Sohn, S. T., Majewski, S. R., Muñoz, R. R., et al. 2007, *ApJ*, 663, 960
- Spencer, M. E., Mateo, M., Walker, M. G., et al. 2017, *AJ*, 153, 254
- Starkenbug, E., Hill, V., Tolstoy, E., et al. 2010, *A&A*, 513, A34
- Strigari, L. E., Bullock, J. S., Kaplinghat, M., et al. 2008, *Nature*, 454, 1096
- Sugiura, N. 1978, *Communications in Statistics - Theory and Methods*, 7, 13
- Suntzeff, N. B., Mateo, M., Terndrup, D. M., et al. 1993, *ApJ*, 418, 208
- Talbot, Raymond J., J., & Arnett, W. D. 1971, *ApJ*, 170, 409
- Tinsley, B. M. 1980, *FCPh*, 5, 287
- Tollerud, E. J., Boylan-Kolchin, M., Barton, E. J., Bullock, J. S., & Trinh, C. Q. 2011, *ApJ*, 738, 102
- Tollerud, E. J., Beaton, R. L., Geha, M. C., et al. 2012, *ApJ*, 752, 45
- Tolstoy, E., Hill, V., & Tosi, M. 2009, *ARA&A*, 47, 371
- van den Bergh, S. 1972, *ApJ*, 171, L31
- Vargas, L. C., Geha, M. C., & Tollerud, E. J. 2014a, *ApJ*, 790, 73 (V14a)
- Vargas, L. C., Gilbert, K. M., Geha, M., et al. 2014b, *ApJL*, 797, L2
- Venn, K. A., Irwin, M., Shetrone, M. D., et al. 2004, *AJ*, 128, 1177
- Walker, M. G., Mateo, M., Olszewski, E. W., et al. 2006, *AJ*, 131, 2114
- Walker, M. G., & Peñarrubia, J. 2011, *ApJ*, 742, 20
- Weisz, D. R., Dolphin, A. E., Skillman, E. D., et al. 2014, *ApJ*, 789, 147
- Weisz, D. R., Dolphin, A. E., Martin, N. F., et al. 2019, *MNRAS*, 1928
- Wheeler, C., Pace, A. B., Bullock, J. S., et al. 2017, *MNRAS*, 465, 2420
- Wolf, J., Martinez, G. D., Bullock, J. S., et al. 2010, *MNRAS*, 406, 1220
- Woo, J., Courteau, S., & Dekel, A. 2008, *MNRAS*, 390, 1453
- Woosley, S. E., & Weaver, T. A. 1995, *ApJS*, 101, 181
- Zucker, D. B., Kniazev, A. Y., Martínez-Delgado, D., et al. 2007, *ApJ*, 659, L21

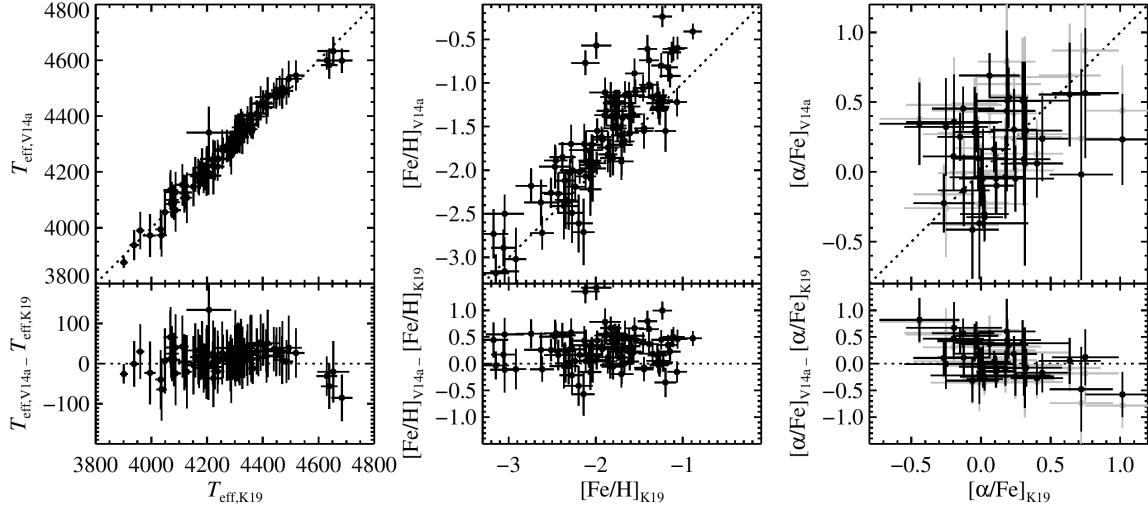


Figure 12. Comparison of our measurements (“K19”) of T_{eff} , $[\text{Fe}/\text{H}]$, and $[\alpha/\text{Fe}]$ with those of V14a. The gray points in the right panel show the “corrected” values of $[\alpha/\text{Fe}]_{\text{V14a}}$, as described in Appendix A.

APPENDIX

A. COMPARISON TO V14A

V14a measured $[\text{Fe}/\text{H}]$ and $[\alpha/\text{Fe}]$ for many of the stars in our sample. The advantage of our study is longer exposures, which resulted in spectra with higher SNR. This appendix compares our measurements to those of V14a. Figure 12 summarizes the comparison. To be consistent with our sample selection, we restrict both samples to measurements with uncertainties less than 0.4 dex. V14a provided a table of abundances. We obtained a table including their measurements of T_{eff} from L. Vargas (private communication).

V14a’s measurements of $[\text{Fe}/\text{H}]$ are significantly higher than ours. The median difference, $[\text{Fe}/\text{H}]_{\text{V14a}} - [\text{Fe}/\text{H}]_{\text{K19}}$, is $+0.25$. The mean difference, weighted by the inverse square of the quadrature sum of the uncertainties, is $+0.30 \pm 0.02$. We cannot readily explain this systematic offset because our two studies used nearly identical techniques to measure abundances. The most significant difference was the set of isochrones used to determine the initial photometric T_{eff} . If this is the source of the difference in $[\text{Fe}/\text{H}]$, there should be an accompanying difference in T_{eff} in the sense that V14a’s measurements of T_{eff} should be larger than ours by roughly 300 K (see Table 6 of Kirby et al. 2010). Figure 12 shows that there is no such offset.

The standard deviation of the differences is 0.32 ± 0.02 . We also computed the standard deviation of the metallicity difference normalized by measurement uncertainty.

$$\text{stddev} \left(\frac{[\text{Fe}/\text{H}]_{\text{V14a}} - [\text{Fe}/\text{H}]_{\text{K19}}}{\sqrt{\delta[\text{Fe}/\text{H}]_{\text{V14a}}^2 + \delta[\text{Fe}/\text{H}]_{\text{K19}}^2}} \right) = 1.53 \pm 0.11 \quad (\text{A1})$$

This quantity would be 1.0 if the measurement uncertainty completely explained the scatter. The fact that it is larger than 1.0 indicates that there is an additional source of discrepancy. Two outliers serve to increase the scatter. When the two points with $[\text{Fe}/\text{H}]_{\text{V14a}} - [\text{Fe}/\text{H}]_{\text{K19}} > +1.0$ are excluded, the quantity in Equation A1 drops to 1.37 ± 0.10 .

V14a measured $[\alpha/\text{Fe}]$ in a manner similar to us. However, they also computed a correction to $[\alpha/\text{Fe}]$. The correction was intended to bring $[\alpha/\text{Fe}]$ into closer agreement with the arithmetic average of $[\text{Mg}/\text{Fe}]$, $[\text{Si}/\text{Fe}]$, $[\text{Ca}/\text{Fe}]$, and $[\text{Ti}/\text{Fe}]$. We reversed this correction so that we could compare like quantities. Nonetheless, we still present V14a’s corrected values as gray points in the right panel of Figure 12.

Unlike $[\text{Fe}/\text{H}]$, there is no significant offset in $[\alpha/\text{Fe}]$ between our two samples. The median difference, $[\alpha/\text{Fe}]_{\text{V14a}} - [\alpha/\text{Fe}]_{\text{K19}}$, is -0.03 . The mean difference, weighted by the inverse square of the quadrature sum of the uncertainties, is $+0.05 \pm 0.05$. The standard deviation of the differences is 0.37 ± 0.03 . When the difference is normalized by the measurement uncertainties, as in Equation A1, the standard deviation is 1.06 ± 0.08 . We conclude that the measurement uncertainties account for the scatter in $[\alpha/\text{Fe}]$.

B. BIAS AGAINST STARS WITH LOW $[\alpha/\text{Fe}]$

In Section 5, we presented the distribution of individual α element ratios with respect to iron (Figure 10). There was an apparent bias against stars with low abundance ratios, especially apparent in $[\text{Mg}/\text{Fe}]$ and $[\text{Si}/\text{Fe}]$. We further investigate this bias with Figure 13, which shows the abundance ratios vs. SNR. The figure also includes measurements in MW dSphs.

There is an increasing dearth of stars with low $[\text{Mg}/\text{Fe}]$ and $[\text{Si}/\text{Fe}]$ as the SNR decreases. The Mg and Si lines used in our spectral synthesis are the weakest among the elements we measured because they generally originate from electron levels with high excitation potentials (~ 5 eV). As a result, they are the first to become undetectable as the SNR and/or abundance drops. Our cut on uncertainty of 0.4 dex further magnifies the bias, which presents as the absence of stars in a wedge in the lower left of the top two panels in Figure 13.

The Ca and Ti lines are stronger and therefore still usable at low SNR. The effect of low SNR is to cause the abundance ratios to fan out rather than to create a wedge that lacks stars. Still, there is some asymmetry in the distribution of abundance measurements at low SNR. Because it is easier to measure high abundances than low abundances, the points tend to scatter high, again leading to a bias against low abundance ratios.

The average $[\alpha/\text{Fe}]$ is based on the union of all the absorption lines of Mg, Si, Ca, and Ti. It is not the average of the abundance measurements, but it is a separate measurement that uses more information than is possible when isolating a single element. As a result, the average $[\alpha/\text{Fe}]$ is less biased at low SNR than the individual α element measurements.

This analysis applies to abundance measurements from spectra obtained with DEIMOS's 1200G diffraction grating. The 600ZD grating accesses a wider wavelength range, including strong Mg lines. Therefore, the biases shown here would not necessarily apply to 600ZD measurements (e.g., Escala et al. 2019a,b).

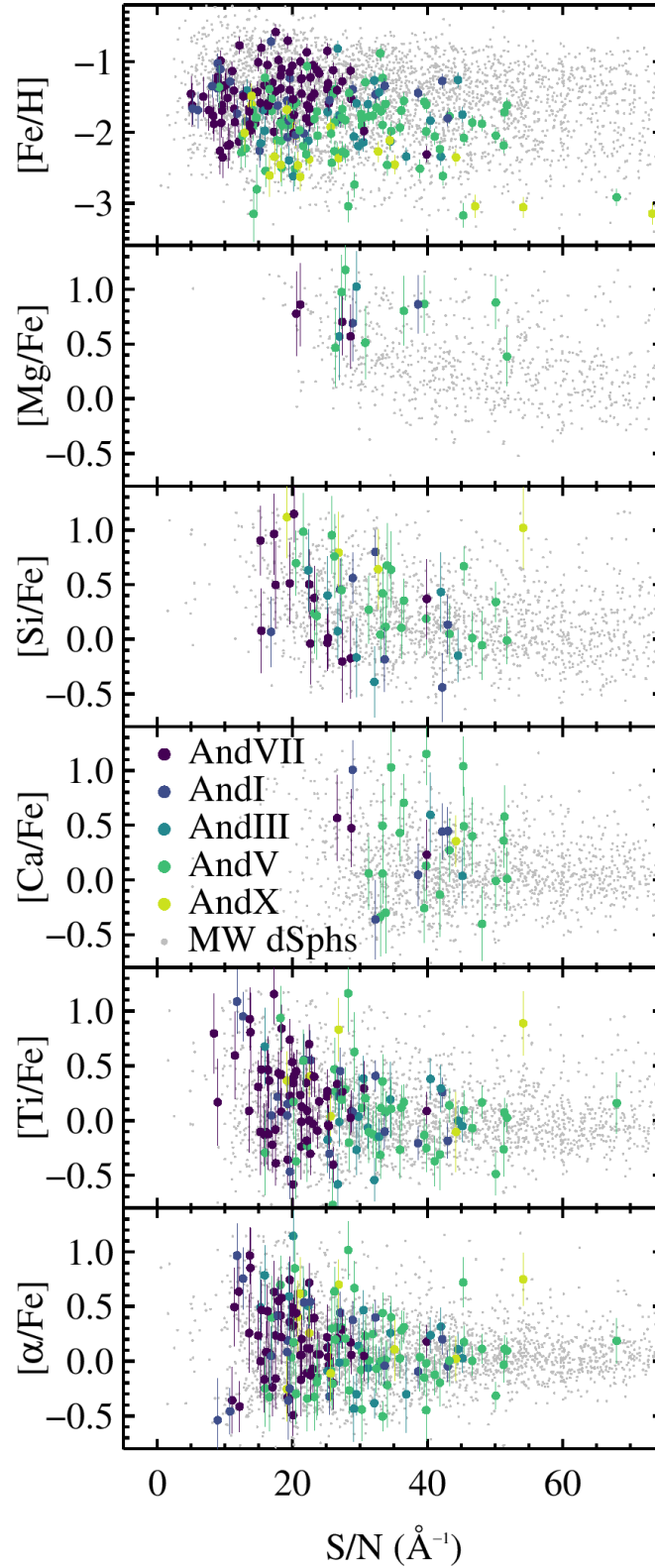


Figure 13. Metallicity ($[\text{Fe}/\text{H}]$, top panel), individual α element ratios (top four panels) and $[\alpha/\text{Fe}]$ (bottom panel) as a function of SNR. The data for the M31 dSphs are the same as shown in Figure 10. This figure also includes measurements in MW dSphs (Kirby et al. 2010). Only measurements with uncertainties less than 0.4 dex are shown.